UNIVERSIDADE DE LISBOA

FACULDADE DE CIÊNCIAS

DEPARTAMENTO DE FíSICA

GATE Model of a SPECT-CT Equipment for Breast Cancer Diagnosis

André Miguel Martins Costa Correia Monteiro

Mestrado Integrado em Engenharia Biomédica e Biofísica
Perfil em Radiações em Diagnóstico e Terapia

Dissertação orientada por:
Dr. Nuno Matela, Instituto de Biofísica e Engenharia Biomédica
Dr. Pedro Almeida, Instituto de Biofísica e Engenharia Biomédica

2016

Acknowledgments

I would like to express my gratitude to those who have contributed for this MEng thesis to be a reality. The comments are written in my mother tongue, Portuguese, due to the fact that some of the people mentioned understand English.

Gostaria de expressar a minha gratidão a todos aqueles que de alguma maneira contribuíram para a conclusão da minha tese de mestrado. Apesar de não ter sido um processo nada fácil, foi extremamente enriquecedor, permitindo reconhecer com cada vez mais força que se queremos ir depressa vamos sozinhos, mas se queremos ir longe vamos juntos.

Em primeiro lugar gostaria de destacar aqueles que desde a 1ª hora estiveram lá para mim, desde o momento em que entrei no curso de Engenharia Biomédica e Biofísica, mas que muitas vezes pus em último lugar, quando nunca deveriam ter deixado de ser os primeiros, enquanto **Pai** e **Mãe**.

Um muito obrigado aos meus dois orientadores o **Professor Pedro Almeida** e ao **Professor Nuno Matela**, nos quais vejo duas excelentes referências tanto a nível profissional numa área tão promissora como a da Engenharia Biomédica, como a nível pessoal.

Em particular, ao **Professor Pedro Almeida** um obrigado por todo o esforço de trazer ao IBEB novas oportunidades com o estabelecimento de diversas parcerias, mas sobretudo e no que diz respeito à minha tese pelas críticas pertinentes que fez sempre que pôde, principalmente quando precisava de descer à Terra com objetivos mais modestos.

Ao **Professor Nuno Matela** fica um obrigado do tamanho do Mundo pelas longas trocas de ideias sobre o trabalho para a dissertação, mas também sobre tudo um pouco. Foi sempre de uma disponibilidade imensa sempre que precisei e sem as suas direcções sobretudo na parte final seria impossível conseguir concretizar este trabalho.

Pessoalmente acho que os dois professores são uma excelente equipa e que me ajudaram da melhor maneira que puderam complementando-se um ao outro.

Ao **Dr. Ricardo Capote**, pela disponibilidade para esclarecer as minhas dúvidas, principalmente quando me encontrava a começar a desenvolver o meu trabalho e no desenvolvimento da parte relativa ao SPECT. A sua ajuda foi vital para que o meu trabalho fosse concretizado.

À **Beatriz Lampreia**, como não poderia deixar de ser por nos receber sempre de sorriso aberto ao toque da campainha e pela força e carinho que nos dava quando precisávamos daquele estímulo.

A todos os professores do IBEB que fizeram parte do meu percurso e que ajudaram a formar-me até este ponto: **Professor Alexandre Andrade**, **Professor Eduardo Ducla-Soares**, **Professor Hugo Ferreira**, **Professor Pedro Cavaleiro Miranda**, **Professor Ricardo Salvador** e **Professora Rita Nunes**.

A todos os meus amigos que acompanharam o meu percurso e que sempre acreditaram em mim, mesmo quando eu mesmo não acreditava nas minhas capacidades.

De entre todos eles, um muito obrigado à **Filipa**, à **Mariana** e ao **Sebastião** por se manterem comigo e transmitirem-me a sua força e carinho e serem cada um à sua maneira uma referência para mim, mesmo quando nem sempre assim o mereci.

Um obrigado também muito especial a todos os meus colegas do **GASNova – Grupo de Acção Social**, sendo que é imperativo dar um obrigado ainda mais especial àqueles nos quais não só mais me apoiei, mas que também, cada um à sua maneira foram também uma referência para mim. Ao **Frederico**, à **Joana**, à **Maria** e à **Teresa** um muito obrigado por fazerem parte da minha vida e em tão pouco tempo terem preenchido tanto do que julgava já perdido.

Aos meus colegas no IBEB, à **Soraia** e ao **João** pelo companheirismo na 1ª fase de desenvolvimento da minha dissertação e ao **Leon**, ao **Nuno** e ao **Pedro** na 2ª fase de desenvolvimento da minha dissertação. Foi importante tê-los também como companheiros ao permitirem-me tirar algumas dúvidas pontuais, mas sobretudo pelas conversas e momentos de descontração.

Um agradecimento também ao **Senhor António** e à **Dona Licínia** por serem como dois pais para mim quando mais precisei e pelas lições de humildade que me moldaram enquanto homem.

Quero também deixar o meu obrigado aos meus **avós Edite**, **Maria** e **Rui** pelo amor e carinho que sempre me deram desde que nasci para ser seu neto.

Por último, gostaria de dedicar esta tese a duas pessoas:

Em primeiro lugar, à minha **bisavó Catarina** pelos seus mais de 100 anos.

Em segundo lugar, à memória do meu **avô Tó** que me motivou a seguir este percurso, aplicando assim o meu interesse pela física à medicina na área da oncologia.

Abstract

Dedicated imaging systems for breast cancer imaging have been comprehensively studied over the past decade. However, since they comprise only one imaging modality these systems are only able to provide either anatomical or functional information of the object of interest. The aim of this work was to simulate and evaluate the implementation of a dedicated system that would be able to extract information regarding both systems in order to provide a complementary diagnostic tool which could be used in inconclusive diagnosis cases.

The proposed solution was to develop two dedicated systems. A dedicated breast computed tomography (DBCT) system that would provide anatomical information and a dedicated single photon emission mammography (SPEM), using convergent collimators, that would retrieve functional information. To create a computer model of this multimodality system, Monte Carlo (MC) simulations were conducted with Geant4 Application for Emission Tomography (GATE) using a simple breast cylindrical phantom with 35 mm radius and 150 mm height, which had 5 mm radius spherical masses composed of aluminum inside it.

For DBCT, the MC simulations were acquired with a PaxScan A® 2520D/CL Amorphous Silicon Digital X-Ray Imager with total dimensions of 192x242x4 mm and 0.508x0.508x4 mm pixels, over 16 projections covering 180º of the phantom, extended to 360º exploiting its cylindrical symmetry. Inside the phantom were placed 5 tumour masses equidistantly along two axis with a tumour mass at the center.

For SPECT, the MC simulations were performed using a dual-head SPECT scanner designed by Dr. Ricardo Capote with 64.0x151.2x188.5 mm as dimensions with pixelated LYSO crystals of 20x2x2 mm and convergent collimators with the same phantom, but with the same 5 mm radius tumour masses placed solely in the x axis.

The MC simulations were conducted in a computer cluster with 4 executions machines.

The projections resultant of the simulations were reconstructed using different algorithms. For DBCT it was used an analytical method of filtered backprojection (FBP) and for SPEM it was used an iterative maximum likelihood expectation maximization (MLEM) algorithm.

To validate the results two non-absolut metrics were calculated to make a relative evaluation of the image quality results. These metrics were only applied to DBCT, since the results obtained for SPEM were not as expected. Contrast and contrast to noise ratio demonstrated that the image quality degrades from the center to the periphery of the DBCT detector.

In conclusion, the acquired results demonstrated the feasibility of breast dedicated systems to, especially for the DBCT system, which yielded the best results, but further development need to be pursued in order to take the most potential of the developed systems which have potential for being used in future studies with more complex and realistic conditions and voxelised phantoms.

Keywords: Breast cancer; Dedicated Breast Computed Tomography; Single Photon Emission Mammography; Flata Panel Detector; Monte Carlo Simulations; Computer Cluster; Filtered Backprojection; Maximum Likelihood Expectation Maximization; Contrast; Contrast to Noise Ratio.

Resumo

O cancro da mama é o tipo de cancro mais diagnosticado nas mulheres, precedido apenas em termos de incidência estatística pelo cancro da pele. No que diz respeito ao número de mortes, o cancro da mama encontra-se também entre os mais importantes relativamente às mulheres, sendo secundado apenas pelo cancro do pulmão em mortalidade.

A deteção precoce de neoplasias na mama ganha assim um papel fundamental de forma a garantir o sucesso do tratamento, melhorando as taxas de sobrevivência daqueles aos quais são diagnosticadas neoplasias mamárias. É nessa deteção que a imagiologia médica se apresenta atualmente como essencial. Não apenas no tremendo esforço nas últimas décadas por melhorar as modalidades imagiológicas já implementadas clinicamente, mas também pelo desenvolvimento de novas que possam adicionar nova informação relevante, especialmente quando perante casos em que o exame médico utilizado não é conclusivo.

Atualmente, a mamografia por raios X é a técnica imagiológica utilizada em prática clínica corrente em rastreios de cancro da mama, rastreios esses que permitem um diagnóstico mais precoce, tendo contribuído nas últimas décadas para um aumento muito significativo das taxas de sobrevivência. No entanto, esta técnica apresenta diversas limitações que podem condicionar o correto diagnóstico dos doentes. Sendo uma técnica que fornece essencialmente informação anatómica e a duas dimensões, apesar de esta oferecer um elevado nível de sensibilidade, a sua especificidade é menor. Isto pode levar a uma menor capacidade de discernir entre lesão benigna e maligna, resultado principalmente da não incorporação de informação metabólica relativa às massas tumorais, bem como, da possibilidade da não identificação de neoplasias, resultado da sobreposição de planos sempre inerente a uma técnica imagiológica apenas a duas dimensões. Desta forma, torna-se necessário recorrer a outras técnicas que providenciem informação adicional sobre as neoplasias detetadas, mas também que possibilitem a visualização a três dimensões, evitando ao máximo procedimentos invasivos desnecessários, tais como biopsias.

Sistemas dedicados para examinar a mama, tirando partido da cada vez maior miniaturização dos componentes eletrónicos essenciais para o desenvolvimento de novos detetores, que possibilitem a aquisição a três dimensões, com uma menor dose de radiação ionizante, surgem com grande expressão em todo o trabalho de investigação realizado no desenvolvimento na área da imagiologia médica. Este incide não só no sentido de restringir ao máximo a zona sobre a qual incide a radiação, mas também no sentido de dar novas ferramentas de diagnóstico para casos onde este é mais difícil, sobretudo quando relativo a mamas de maior densidade.

Nesse sentido, e como forma de obter informação complementar, a tomografia computorizada (TC) por raios X – que fornece informação anatómica tridimensional – e a tomografia computorizada por emissão de fotão único (TCEFU), que ao ser aplicada em específico ao exame da mama toma o nome de mamografia por emissão de fotão único (MEFU) – que providencia informação funcional tridimensional – são duas modalidades que podem ser utilizadas em sistemas dedicados, como forma de meio de diagnóstico complementar, combatendo assim as limitações inerentes à mamografia.

Nesta dissertaçãio, é apresentada uma solução que, por meio da incorporação de dois sistemas dedicados das modalidades acima mencionadas, tem como objetivo a implementação através de simulações de Monte Carlo (MC), com recurso ao programa *Geant4 Application for Emission Tomography* (GATE) que possui a sua própria linguagem macro dedicada para desenvolvimento de simulações de MC. Este programa, pela incorporação de outros programas externos a si (CLHEP, ROOT, *for GEometry ANd Tracking* (Geant4)), permite projetar simulações complexas, combinando a vantagem da utilização do Geant4 - com os seus processos físicos bem validados e geometria sofisticada

- com funcionalidades próprias para tomografia de emissão. Uma vez que o GATE utiliza uma linguagem própria, a necessidade de uma programação de outra forma exaustiva em C++ é eliminada, necessidade essa que seria uma realidade caso fosse usado o Geant4 diretamente.

Utilizando um fantoma cilíndrico com 35 mm de raio e 150 mm de altura, com composição semelhante a tecido mamário, foram realizadas simulações para ambas as modalidades, onde foram colocadas massas tumorais compostas por alumínio, ao longo de várias posições no mesmo eixo, de forma a avaliar a qualidade da imagem conseguida através da aquisição por parte destes equipamentos.

A simulação de TC foi efetuada colocando no interior do fantoma 5 massas tumorais com 5 mm de raio equidistantes entre si ao longo do eixo do x e do z, resultando numa disposição em L. A aquisição foi adquirida em 16 projeções de 10 s a 180º do cilindro, totalizando um tempo total de 160 s. De forma a englobar 360º em torno do fantoma as projeções obtidas foram posteriormente espelhadas e incorporados no resultado final, aproveitando a simetria simétrica do mesmo. A disposição em L permitiu assim verificar a qualidade da imagem reconstruída relativamente a dois tipos de distância em relação ao centro do detetor de 192x242x4 mm, compostos por pixéis quadrangulares de dimensões 0.508x0.508x4 mm.

Para o MEFU foi utilizado o detetor desenvolvido pelo Dr. Ricardo Capote, utilizando os mesmos parâmetros de aquisição utilizados no trabalho desenvolvido pelo Dr. Ricardo Capote, composto por duas câmaras gama de 64x151.2x188.5 mm, constituídos por cristais pixelizados de LYSO, sendo que cada um tinha 20x2x2 mm. De forma a direcionar a radiação gama a detetar estas câmaras utilizavam também colimadores convergentes. Tal como no trabalho do Dr. Ricardo Capote foram feitas simulações com 64 projeções por câmara ao longo de uma órbita circular, totalizando 10 minutos de duração de exame. No entanto, ao contrário do que aconteceu para a modalidade de TC, apenas se realizaram simulações onde foram inseridas no interior massas tumorais que variavam a sua posição relativa, apenas em uma coordenada.

Os ficheiros finais da TC foram posteriormente processados com recurso a um ficheiro de C++, utilizando comandos próprios do programa ROOT, de forma a extrair as projeções da imagem, sendo posteriormente feita a sua reconstrução tridimensional utilizando o algoritmo analítico Filtered BackProjection (FBP), implementado no MATLAB®.

De forma similar, os resultados da MEFU foram tratados por um ficheiro .C que extraía as contagens nos detetores a partir do ficheiro resultado das simulações, sendo estes posteriormente reconstruídos tridimensionalmente com recurso ao algoritmo iterativo *Maximum Likelihood Expectation Maximization* (MLEM).

Após ser feita a reconstrução de ambas as modalidades, os resultados foram validados por meio da utilização de métricas não-absolutas relativas apenas para a TC, nomeadamente o contraste e o rácio entre o contraste e o ruído. Os resultados obtidos demonstraram uma degradação da imagem do centro do detetor para a periferia, degradação essa que seria o expectável tendo em conta a geometria de toda a simulação.

Desta forma, foram implementados ambos sistemas com a visualização de um fantoma cilíndrico simples. As métricas utilizadas para avaliação na TC comprovaram a sua viabilidade. No entanto, o desenvolvimento destes sistemas, teve como principal objetivo permitir a possibilidade de ser realizada uma futura implementação que incorporasse as duas modalidades, dando assim dois tipos de informação complementares no mesmo exame. De modo a que o modelo pudesse ser utilizado em ocasiões futuras, e até como ponto de referência para a utilização do próprio GATE em qualquer projeto, a metodologia empregue foi descrita exaustivamente. Espera-se que o modelo elaborado no decorrer deste trabalho, apesar dos resultados de MEFU não terem sido os melhores, possa servir como ponto de partida para novos estudos. Estudos futuros poderão incorporar algoritmos mais complexos de reconstrução, ou ainda efetuar a adaptação das simulações de MC para utilização computação em GPU,

utilizando fantomas voxelizados, podendo assim diminuir drasticamente o tempo de computação das simulações.

Palavras-chave: Cancro da Mama; Tomografia Computorizada; Mamografia por Emissão de Fotão Único; Reconstrução de Imagem; Simulações de Monte Carlo; *Geant4 Application for Emission Tomography*; *Filtered Back Projection*; *Maximum Likelihood Expectation Maximization*; Contraste; Rácio entre o Contraste e o Ruído

Contents

List of Figures

List of Tables

Acronyms and Abbreviations

2D – two dimensional
3D – three dimensional
^{99m}Tc – Technetium-99m
ADC – Analogue to digital converters
APD – Avalanche photodiode
ART – Algebraic reconstruction technique
a-Se – Amorphous selenium
a-Si – Amorphous silicon
BSGI – Breast Specific Gamma Imaging
CT – Computed Tomography
CZT – Cadmium zinc telluride
DBCT – Dedicated breast computed tomography
DBT – Digital breast tomosynthesis
DCE-MRI – Dynamic contrast enhanced - magnetic resonance imaging
DCIS – Ductal carcinoma *in situ*
DTI-MRI – Diffusion tensor imaging - magnetic resonance imaging
ET – Emission tomography
FBP – Filtered backprojection
FOV – Field of view
FPD – Flat panel detector
FWHM – Full width at half maximum
GATE – Geant4 Application for Emission Tomography
Geant4 - for GEometry ANd Tracking
IBEB – Instituto de Biofísica e Engenharia Biomédica
IDC – Invasive ductal carcinoma
LCIS – Lobular carcinoma *in situ*
LCRNG – Linear congruential random number generator
LFRNG – Lagged Fibonnaci random number generator
LOR – Line of Response
MBI – Molecular breast imaging
MC - Monte Carlo
MCNP – Monte Carlo N-Particle
MLEM – Maximum likehood expectation maximization
MRI – Magnetic resonance imaging
NaI(Tl) – Sodium iodide doped with tallium
OSEM – Ordered subset expectation maximization
PEM – Positron Emission Mammography
PENELOPE – PENetration and Energy LOss of Positrons and Electrons
PMT – Photomultiplier tube
PRNG – Pseudo-random number generator
PSRF – Point source response function
RF – Radio-frequency
ROC – receiver operating characteristic
ROR – Radius of rotation

SGE – Sun Grid Engine
SimSET – Simulation System for Emission Tomography
SIRT – Simultaneous Iterative Reconstruction Technique
SNR – Signal to noise ratio
SPECT – Single Photon Computed Tomography
SPRF – Single pixel response function
TFT – Thin film transistor
US – Ultrasound

1. Introduction

Breast cancer is a public health problem with an increasing incidence rate amongst women, being one of types of cancer with higher mortality numbers [1].

The successful implementation of screening programs with X-ray mammography led to a reduction in mortality, being considered as the "gold standard". However, despite its importance in the past two decades, this imaging modality has several limitations. Since it is performed in two views of each breast it does not provide three dimensional (3D), but only two dimensional (2D) information, which could cause tissue overlapping. Adding to this major problem, the inability to retrieve functional information – which could be important in early cancer stages – could also difficult the differentiation between benign and malign tumour cells [1,2].

To address this isssues fully 3D imaging modalities are beginning to emerge, such as Computed Tomography (CT) or Single Photon Emission Computed Tomography (SPECT) [3, 4]. CT provides excellent and accurate anatomical information and SPECT offers the ability to evaluate functional data at a molecular level. Especially when dealing with dense breasts, doing only a mammogram exam can lead to inconclusive diagnosis. Anatomical 3D imaging modalities, as well as other complementary techniques may allow a more accurate diagnosis, staging, and treatment response of neoplasms.

Adding to the fact that the different types of cells which constitutes the breasts are highly sensitive to radiation, breasts are anatomically localised in the thoracic cavity, close to the heart and other sensitive organs. Therefore, the amount of radiation to which the patients are exposed should be lower than other types of exams. Hence, the need for the creation of dedicated systems that could reduce the amount of radiation as possible come as natural development in the actual paradigm [5, 6].

The combination of two imaging modalities, one anatomical or structural and other functional, can enhance the modalities strengths presented when working alone, as well as removing some of its weakness(es).

Amongst several imaging modalities, SPECT and CT were the modalities chosen to make a *Geant4 Application for Emission Tomography* (GATE) model which could be used to test and evaluate the feasibility of a dedicated dual-modality equipment.

The project was inserted in the *Medical Imaging and Diagnosis group*, which investigates several topics in image processing, being breast imaging processing one of them. The project was conducted at IBEB under the supervision of professor Pedro Almeida and professor Nuno Matela.

This thesis is structured in several chapters. Chapter 1 contextualises the scope of the work. Chapter 2 will address the different types of imaging modality, ending with a subchapter concerning multimodality imaging. Chapter 3 will focus on theoretical aspects regarding CT and SPECT techniques, tomographic imaging reconstruction techniques and Monte Carlo (MC) simulations. Chapter 4 will describe the experimental methods in detail. Chapter 5 will present the results and correspondent discussion. Finally, the last chapter will concern the conclusions and final remarks that were derived from completion of this project.

2. Breast Imaging

2.1. Clinical Background

The female breast has many component parts, including lobules (milk-producing glands), ducts (tubes that carry milk from the lobules to the nipple), connective (fibrous) tissue that surrounds the lobules and ducts, fat, and skin as represented in Figure 2.1 [7].

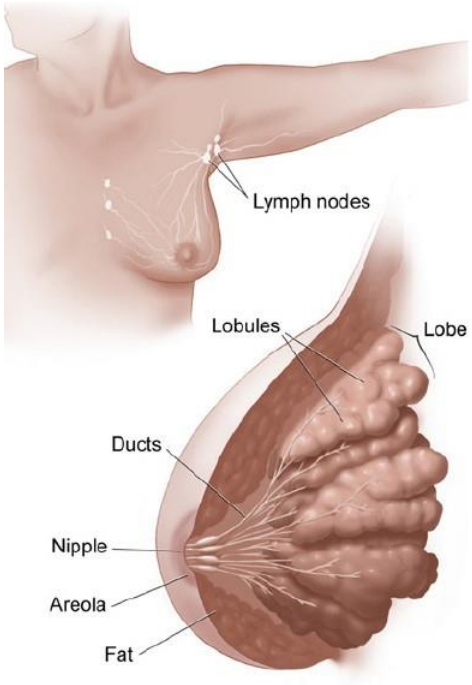

Figure 2.1 - Breast anatomy. It also shows lymph nodes near the breast. Adapted from [8].

Each breast has a number of sections (lobules) that branch out from the nipple. Each lobule holds tiny, hollow sacs (*alveoli*). These lobules are linked by a network of thin tubes (ducts). If the female is breast-feeding, ducts carry milk from the *alveoli* toward the dark area of skin in the centre of the breast (areola). From the areola, the ducts join together into larger ducts ending at the nipple (see figure 2.1).

Spaces around the lobules and ducts are filled with fat, connective tissue and ligaments. On average, breasts consist of 70% glandular (ductal and lobules) tissues and 30% fat. The amount of fat in the breasts largely determines their size, as well as its density, which decreases with the increase of fat percentage [8].

Breast cancer can be considered a group of diseases in which abnormal cells divide without control originated within the breast, and that often later invade the surrounding tissues or metastasize to distant areas of the body. The most common origin of breast cancer is in the cells that form the ducts (ductal cancers) [7], but can also be originated from the cells that form the lobules (lobular cancers) [9] and a small number in other surrounding tissues.

Cancers that have not spread beyond their localized area are called *in situ*, for example ductal carcinoma *in situ* (DCIS) and lobular carcinoma *in situ* (LCIS). However, breast cancer appears more frequently as invasive cancer. Contrary to *in situ*, in invasive cancer the tumour cells do not circumscribe

to breast tissues, but spread to other types of tissues in other parts of the body. The most commonly diagnosed breast cancer is invasive ductal carcinoma (IDC), which is originated in the ducts, accounting for approximately 80% of invasive breast cancers [8].

2.2 Health Statistics

Breast cancer is the most common cancer among women, except for skin cancer, with 1.67 million new cases of breast cancer occurring among women worldwide in 2012 and 521900 resulting deaths [10][11]. Every 1 in 8 (12%) women in the United States will develop invasive breast cancer during their lifetime [7]. In 2016, the appearance of 246660 new cases and 40450 deaths from breast cancer are the estimates. In Portugal, the deaths from malignant breast cancer raised from 1504, in 2008, to 1663, in 2012, per 100000 women [12].

While the number of detected incidences has increased over the last twenty years, survival rates have also steadily increased, due to advances in breast cancer detection and improved adjuvant treatment options [8, 13]. The 5-year relative survival for localized breast cancer (stages 0-I) has increased to nearly 100% today. This number drops to 93% if the cancer has spread regionally to the lymph nodes (stage IIA), and down to 22% for women with distant metastases (stage IV) [8]. Thus, early detection of breast cancer is vital, because treatment of small tumours allows for smaller surgeries, with increased breast conservation and smaller chance of recurrences.

2.3 Breast Imaging Modalities

Over the past two decades, the mortality due to breast cancer has seen a reduction in mortality of about 80%. This result is mainly related to the introduction of screening programs based on the usage of mammography [1, 2]. Although X-ray screening mammography has saved many lives and is considered the “gold standard” it has several limitations.

In clinical practice, X-ray mammography is commonly used in screening programs as imaging modality, however when there are some symptomatic cases, other techniques might be used. These techniques have the objective to correctly identify all the individuals who have cancer, i.e. high sensitivity, and correctly identify individuals who do not have cancer, i.e. high specificity. The imaging techniques that are implemented are 2D or 3D and can be divided in two types: anatomical and functional. Anatomical imaging has a high spatial resolution and sensitivity, but lower specificity since image quality can be affected by breast density. Functional imaging, on the contrary, is not dependent of breast density and has a high specificity in detecting tumours, especially distinguishing between benign and malignant tumours, but a poor spatial resolution.

Since mammography is a 2D representation from a 3D structure, which leads to the superimposition of tissues and limits its effectiveness, especially in women with dense breasts, the need for new types of imaging techniques that could overcome these limitations arises either by using functional or anatomical imaging. These imaging techniques, current or proposed ranged from digital breast tomosynthesis (DBT), dedicated breast computed tomography (DBCT), magnetic resonance imaging (MRI), ultrasound (US), scintimammography, positron emission mammography (PEM) and SPECT. Table 2.3.1 shows some characteristics of each imaging technique above mentioned.

Imaging Modality	2D or 3D	Inherent Contrast	Sensitivity/Specificity	Resolution (mm)	Major Problem
Mammography [14]	2D	Photon attenuation differences in breast tissue	0.88/0.60	0.05	Overlapping tissues
DBT [14]	Pseudo 3D	Photon attenuation differences in breast tissue	0.93/0.64	0.07 (detector pixel)	Out of plane blurring
DBCT [15]	3D	Photon attenuation differences in breast tissue	0.87/0.88	0.388 (reconstructed voxel)	Poor chest wall coverage
DCE-MRI [16, 17, 18]	3D	Contrast enhanced blood flow shows areas of abnormal angiogenesis	0.93/0.74	0.625 (sampled voxel)	Expensive; time consuming
US [18, 19]	2D, 3D	Differences in speed of sound in breast tissues	0.78/0.89	0.4	Poor image quality
Scintimammography with ^{99m}Tc (Dual-Head, CZT) [20]	2D	Uptake tracer in mitochondria which increase metabolic activity	0.75(0.90)/ 0.83	2.5 (detector pixel)	Radiation to whole body
PEM with ^{18}FDG [21, 22]	3D	Mimics glucose cells preferred energy source; more energy requires more ^{18}FDG	0.86/0.91	3	Radiation to whole body

Table 2.3.1: Inherent contrast, sensitivity and specificity, resolution and limitations of current and proposed screening and diagnostic breast imaging modalities.

2.3.1 X-ray Mammography

X-ray mammography is an imaging modality which uses low-energy X-rays (usually around 30 keV) to examine the human breast, which is currently the main screening modality for the general population and considered the "gold standard" for early breast cancer detection, because it is relatively inexpensive, low in radiation dose, widely available and has proven its clinical value over many years of use [1, 2].

X-ray mammography, however, has many known limitations including a low positive predictive value and frequent false negatives. In addition, mammography has a very limited ability to detect pre-cancerous changes in women with dense breast tissue due to the radiographically dense overlapping structures [23, 24]. An additional disadvantage is that mammography causes discomfort due to breast compression.

Mammogram results are often expressed in terms of the Breast Imaging Reporting and Data System (BI-RADS) Assessment Category, often called a "BI-RADS score." The categories range from 0 (Incomplete) to 6 (Known biopsy – proven malignancy). In the United Kingdom, mammograms are scored on a scale from 1-5 (1 = normal, 2 = benign, 3 = indeterminate, 4 = suspicious of malignancy, 5 = malignant) [25].

While the overall sensitivity of mammography for detecting breast cancers has been reported as ranging from 71% to 96% [26], that value significantly drops to values ranging between 30% and 60% in women with dense breasts [27, 28]. Concerning specificity, a study from David Gur et al. [29] reported a result of 60% without distinguishing fatty from dense breasts.

2.3.2 Emerging Breast Modalities

The well-known limitations of mammography, which were previously mentioned, have led to the investigation of alternative or complementary techniques aiming to aid breast diagnosis and staging, reduce unnecessary biopsies, contribute to an earlier lesion detection, especially with smaller lesions, which if undiagnosed, might progress into tumours of larger dimensions.

DBT is an emerging dedicated breast imaging modality that creates a limited-tomographic pseudo-3D image of the breast, by taking multiple X-ray images in a short arc above the breast [30–32]. The breast is positioned in the same way as in a conventional mammogram with slightly breast compression, to keep the breast in a stable position during the procedure. In an experimental clinical series conducted by Svahn et al. [33] compared the accuracy of one-view DBT to a two-view mammography and reported approximately 90% and approximately 79%, respectively, for sensitivity values. Early results are encouraging, yet it remains to be seen what the future clinical role of DBT in breast cancer diagnosis would be.

DBCT is capable of imaging the breast without compression and can provide high resolution 3D images. By acquiring X-ray projection images over a full 360º angular range, DBCT has the capability of providing a 3D volume with detailed anatomical information of the breast. 3D volumetric data remove overlapping structures and thus should more easily illustrate anomalies in soft tissue, such as a tumour, when compared to other existing modalities [31]. A study performed by Binghui Zhao et al. [3] demonstrated that DBCT, with low X-ray dose in a safe range, outperformed X-ray mammography both in sensitivity (86.6% against 77.7%) and specificity (87.5% against 72.5%).

Breast US is also a promising adjunct to screening mammography [34–36], particularly for discriminating between benign cysts and malignant tumours [37, 38]. US provides real-time images independently of density, through the use of non-ionizing ultrasonic waves. Results of a recent study conducted by Berg et al. showed increased sensitivity when using ultrasound and mammography in combination versus using mammography alone (77.5% vs. 50%), but with a drop in specificity (89%

vs. 95%), because some tumours cannot be detected with only one of the modalities [39]. Despite that, breast US has been found to be very good at identifying cysts, especially since the appearance of elastography, it has not been shown to outperform MRI or scintimammography for diagnosis of malignant disease [35, 40-42].

Unlike mammography, DBT or DBCT, dynamic contrast enhanced-magnetic resonance imaging (DCE-MRI) is a 3D volumetric imaging technique which does not use ionizing radiation and is insensitive to breast density [43]. It uses specialized radio-frequency (RF) coils to measure the temporal flow characteristics of an MRI contrast agent (usually gadolinium-based) through tissue by rapidly acquiring MRI images during the injection of the contrast agent. By comparing the values of relaxation time it is possible to identify suspicious volumes, since they have higher relaxation times than normal surrounding tissue, in order to diagnose breast cancer. In literature, the reported sensitivity of DCE-MRI for breast cancer ranges from 77% to 100% and specificity is within 42% to 96% [44-49]. Preliminary diffusion tensor imaging - magnetic resonance imaging (DTI-MRI) studies of the normal breast [50-52] and breast lesions [53-55] have also been reported with results of 95.6% for sensitivity and 97.7% for specificity [56]. The high cost per scan and limited availability have slowed DCE-MRI and DTI-MRI clinical adoption to the general population screening.

Nuclear medicine molecular imaging methods have also been adapted for detection and diagnosis of breast cancer. These techniques are almost not affected by breast density and are powerful complements to structural imaging modalities (e.g. mammography and DBCT), because of their ability to provide functional information that can help differentiate malignant from benign tumours. Small concentrations of injected radiotracers are imaged, demarcating malignant – which have a higher metabolic activity – from benign tumours based on the metabolic uptake of the radiotracer [56, 57]. It is well accepted that molecular changes can occur before structural deformations, and nuclear medicine imaging has the ability to distinguish these subtle changes [58]. This aspect can be important not only in detecting early stages of cancer, but also in staging patients who have already being diagnosed with cancer. However, adding to the fact that not only the scanners are more expensive than mammographs, but also the additional cost of the radionuclides, as well as a higher radiation dose, make these imaging modalities not ideal for screening mass populations.

We can distinguish different modalities in nuclear medicine imaging by the type of emission of the radionuclide, which could be either photon or positron emission. In positron emission, the image is formed when two photons of 511 keV are emitted from the annihilation of the emitted positrion – resultant from the radioactive decay – with an electron. Photon emission results from a radionuclide undergoing gamma decay, in which detector systems will acquire photon counts. Scintimammography (2D) and SPECT (3D) are based on photon emission and PEM (3D) is based on a positron emission procedure.

Scintimammography is a planar single photon imaging technique, which until the last 10 to 15 years, has been acquired with whole body gamma cameras. During this period, scintimammography was found to be useful in diagnosing breast cancer in women with dense or fibrous breasts [59]. Early scintimammography studies, using conventional whole-body gamma cameras and no breast compression for prone lying women, yielded a sensitivity and specificity of approximately 85% [60, 61], but sensitivity dropped significantly for tumors smaller than 1 cm in diameter [62].

If many single photon emission images are acquired from different views around a volume, then they can be reconstructed to form a 3D SPECT image, improving the accuracy of the diagnosis. Dedicated breast SPECT has been investigated for both clinical cameras [62–65] and dedicated systems [66–68], yielding improvements in lesion contrast and signal to noise ratio (SNR) by up to a factor of three [62, 69], mostly due to the reduction of the radius of rotation (ROR), which is inversely proportional to contrast, resolution and image quality. A study conducted by Sharjeel Usmani et al. [70] with 26 patients reported values for sensitivity and specificity of 89% and 87.5% for SPECT exams.

Finally, PEM has also been used as a complementary technique for breast cancer diagnosis. The first system was proposed in 1994 [71]. A pre-clinical trial of this camera in 16 subjects with suspicious breast lesions yielded a sensitivity of 80%, a specificity of 100% and a diagnostic accuracy of 86% [72]. The first commercially available PEM scanner uses two sets of scanning planar detectors and women are imaged with breast compression which is also important in immobilizing the breast (Naviscan PET Systems, San Diego, CA) [73]. A multi-center trial of this device in 77 women reported a lesion detection sensitivity of 90% and a specificity of 86% [21].

2.4 Multimodality Imaging

Multimodality imaging is achieved when two or more biomedical imaging techniques are combined in a single output. This could either be obtained by image fusion of different scans using only sophisticated software either by using hybrid systems, which are composed by two or more systems that are operated simultaneously or sequentially [74].

It was not until the late 1980s that image fusion was explored systematically. By identifying landmarks or fiducials or by optimising a metric based on intensity values these methods achieved a great success when aligning images for the brain, but the results were disappointing for other parts of body with a higher number of possible degrees of freedom, therefore increasing the complexity of the transformation [75].

In the early 2000s, the development of new hybrid imaging systems, encompassing two different modalities in the same system, ensured accurate alignment, since both were acquired in the same reference frame. The development of PET/CT and SPECT/CT systems in 2001 and 2004, allowed to explore the strengths of anatomical and functional images, improving not only the accuracy of the diagnosis, but also assessing treatment response at the utmost point of replacing PET standalone systems for PET/CT in current clinical practice [74].

The motivation for combining CT with functional imaging such as PET and SPECT was the particular need to improve spatial resolution in functional imaging, providing the appropriate anatomical context to detected lesions and eliminating the need for a lengthy transmission scan to account for attenuation correction. This is possible due to the fact that CT is basically a map of attenuation coefficients, allowing to generate the attenuation correction factors by simply scaling the CT image data to the functional imaging energies. In addition, CT can also be used to correct partial volume effect, therefore reducing imaging artifacts that otherwise would be present [76].

For SPECT, CT has an additional importance since the attenuation correction factors provide depth information that SPECT doesn't provide. In addition, SPECT has great potential, because it has access to a much broader range of biomarkers and radiopharmaceuticals than PET, with highly specific tracers to certain diseases.

Specifically, concerning breast imaging, the miniaturisation of the components recently made possible dedicated hybrid breast imaging devices such as SPECT/CT and PET/CT. Due to the fact that breast is one of the body regions most susceptible to ionizing radiation, the design of dedicated systems is extremely important, since they are able to provide similar or even better performances than whole-body systems at a fraction of the dose. Patient comfort is also improved by optimising the equipment design, allowing lower scan times [76].

In addition to SPECT/CT and PET/CT, other multimodality imaging devices are being developed such breast CT/PEM, SPECT/DBT and US/PET [76]. In the last years, there has been an increasingly interest in PET/MRI and SPECT/MRI systems, but the technical problems experienced in the early prototypes that worked with PMTs, which are sensitive to magnetic fields, slowed the expansion of this research area. However, despite the fact that we have currently simultaneous

commercial PET/MRI systems since 2011, the applicability of this devices towards the breast imaging yet remains to be proven [76].

The following chapter will address the theoretical concepts involved for each imaging modality, a brief description of the reconstruction process and how MC simulations are used to test the model of the dedicated breast SPECT/CT system which was developed.

3. Theoretical Concepts

3.1 Computed Tomography

Tomography derives from the Greek words “tomos” meaning “slice” or “section” and “graphia” meaning “describing” [77].

After the accidental discovery of the X-ray radiation by the German scientist Wilhelm Conrad Rontgen in 1895, Dr. Allan MacLeod Cormack of Tufts University, Massachusetts and Sir Godfrey Newbold Hounsfield of EMI Laboratories, United Kingdom developed an imaging technique named Computed Tomography. From Cormack’s theoretical idea in the late 1950s to Hounsfield’s development of a practical device in the late 1960s, Hounsfield was able to present in April 1972, in a seminar at the British Institute of Radiology, the results he had obtained using the EMI scanner (CT scanners were known as EMI scanners, because it was the name of the company) and descriptions of the device appeared in many publications. Both scientists were later in 1979 awarded the Nobel Prize in Physiology or Medicine and Hounsfield also received a knighthood for his work [78][79].

In the 1980s the development of this imaging technique seemed to reach its peak and during this decade almost none technological progress was seen. With the introduction of spiral CT in 1989 by Kalender et al. [80] and subsequent developments in X-ray detector and scanner technology have led to a revitalization of interest in CT, making it an essential imaging diagnostic technique, not only by the increased acquisition velocity, essential to new cardiological applications, impossible with other imaging techniques, but also new applications of CT itself as interventional and intra-operative imaging in the future [80].

The fundamental principle behind CT states that density of the tissue passed by X-rays can be measured from the calculation of the attenuation coefficient. Represented in figure 3.1.1, with an X-ray emitter and a detector placed diametrically on the opposite side, the CT scanner captures cross-sectional images at different angles, allowing to retrieve the information on the depth, conferring a 3D visualisation of the volume that is being imaged [81].

Although CT is considered as the principle origin for of human exposure from artificial artificial radiation exposure, the broad spectre of CT applications and the increasing number of scanners installed also contributed to its adoption in several medical areas due to this rapid propagation and versatility. Particularly, between 1999 and 2008, the number of CT machines in Portugal increase 40% to a total of 291 machines, roughly 27.6 machines per million inhabitants [82].

Lower acquisition times and the galloping miniaturisation of the system components allowed for the development of dedicated systems with a substantially lower dose of radiation, such as DBCT, equivalent to 4-5 mammography views, increasing diagnostic and treatment accuracy by providing 3D information, as well as a complete attenuation coefficients map, which was not obtained with a conventional mammography [33].

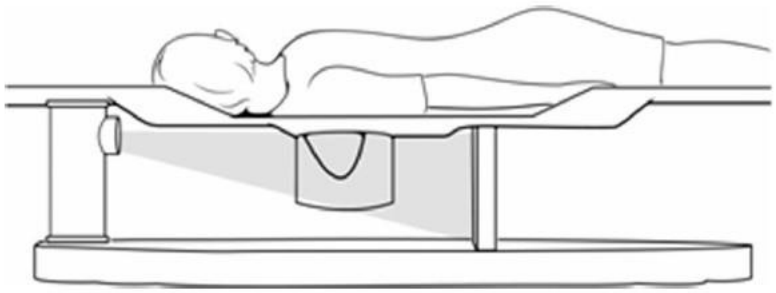

Figure 3.1.1: Schematic representation of breast CT and subject positioning. Image obtained from [33].

The following sections will describe the important physics background in X-ray production (section 3.1.1) and the main physical components of a dedicated CT machine: the X-ray tube (section 3.1.2) – where the X-rays are generated – and the flat panel detector (section 3.1.3) – which detects the photons which were not absorbed by the patient body.

3.1.1 X-ray Production

The X-rays used for medical imaging are produced when high-energy electrons interact with a metal target and convert their energy into electromagnetic radiation. The X-ray tube consists mainly of a tungsten filament, the cathode, with negative charge and a rotating tungsten-rhenium target, the anode, with positive charge. A high current flowing through the filament, creates a cloud of electrons, in a process known as thermionic emission. An external power source supplies a high voltage across the anode and cathode junction, accelerating the electrons across the junction, forming a focused electron beam that bombards the anode. The kinetic energy of the electrons is then converted by three processes. One of them converts the energy into heat, approximately 99%, and the others produces X-rays, that could be either characteristic radiation or Bremsstrahlung radiation, making the efficiency of the process only 1% [83].

3.1.1.1 Photon Interactions with the Matter

When traversing matter, photons can be scattered, absorbed or penetrate without any interaction. There are three photon interactions with matter which are important in the energy ranges of X-rays and nuclear medicine radiation measurements: photoelectric effect, coherent or Rayleigh scattering and Compton or inelastic scattering.

3.1.1.1.1 Photoelectric Effect

Photoelectric effect – as represented in figure 3.1.1.1.1.1 – describes the process in which an inner shell electron in an atom completely absorbs the energy of an incident photon, removing the electron from its orbital. The kinetic energy of the ejected electron (E_e) is equal to the incident photon energy (E_o) minus the binding energy (E_b) of the orbital electron [8]:

$$E_e = E_o - E_b \qquad \text{(Eq. 3.1.1.1.1.1)}$$

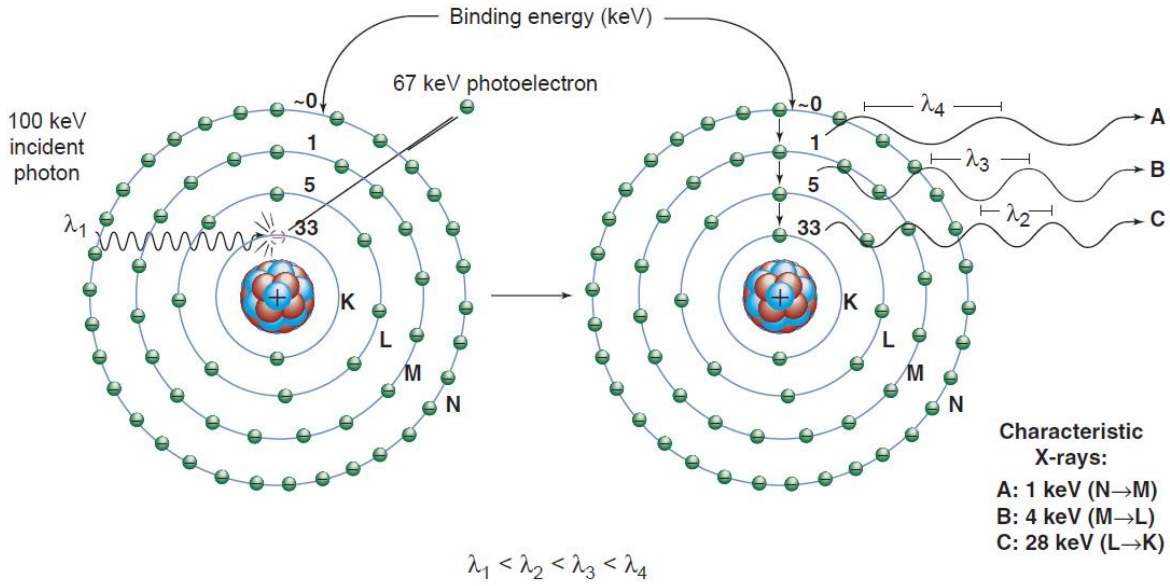

Figure 3.1.1.1.1.- Photoelectric effect. The scheme represents an incident 100 keV photon which causes the ejection of an electron with 67 keV of kinetic energy on the left. On the right electrons on the outer orbitals occupy the inner orbitals, emitting characteristic X-rays with energy correspondent to the difference in the binding energies of the different orbitals. Image obtained from [84].

In order for photoelectric effect to occur, the incident photon energy must be at least equal to the binding energy of the electron that is ejected. This process predominates when lower energy photons interact with high Z materials, such as tungsten. Below 50 keV, photoelectric effect in soft tissue plays an important role in medical imaging, causing an amplification of differences in attenuation between tissues resulting in an improvement of image contrast.

3.1.1.1.2 Rayleigh Scattering

Rayleigh or coherent scattering takes place when a photon interacts directly with an atom as a whole. Due to the large mass of the atom, the photon is re-emitted in a different direction while retaining all of its original energy, as represented in figure 3.1.1.1.2.1. No energy is converted into kinetic energy, and ionization does not occur.

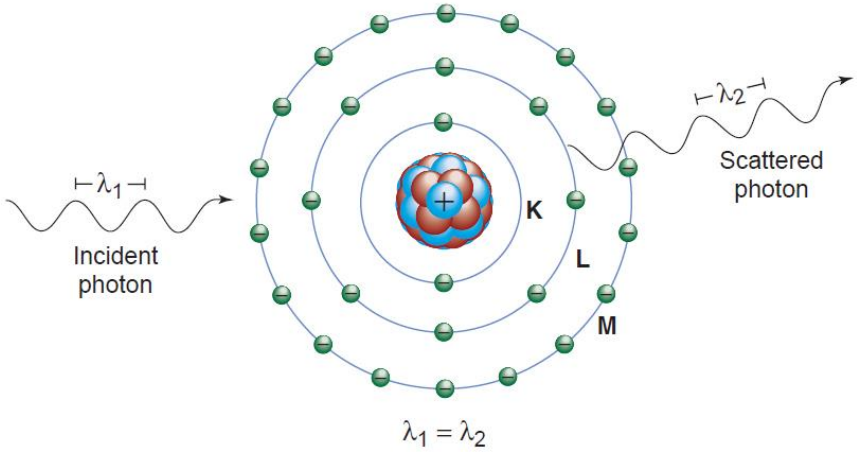

Figure 3.1.1.1.2.1. - Rayleigh scattering. Image obtained from [84].

Coeherent (Rayleigh) scattering plays only a minor importance in low-energy CT imaging (accounting for 10-15% of photon interactions in water at 36 keV) [58]. In medical imaging, detection of scattered X-ray degrades the image quality, however the probability for this process to occur in the diagnostic energy range is low.

3.1.1.1.3 Compton Scattering

Compton scattering or inelastic scattering is the most important interaction of X-ray and γ-ray photons in the diagnostic energy range. This interaction is most likely to occur when a photon interacts with a loosely bound outershell orbital electron of an atom in the material. Part of the energy of the photon is transferred to the recoiling electron, which is ejected from the atom, and the photon is emitted at a scattering angle θ (see figure 3.1.1.1.3.1).

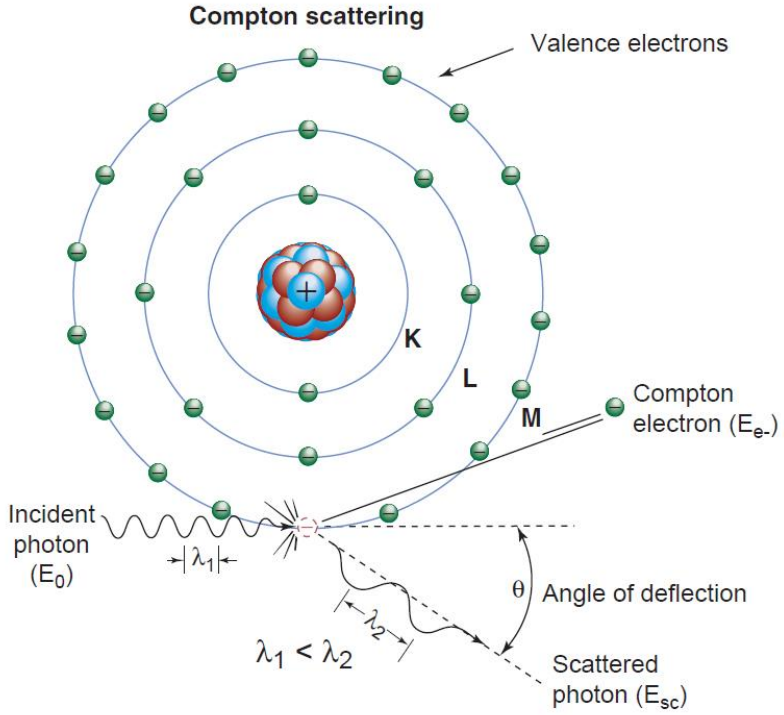

Figure 3.1.1.1.3.1. - Compton scattering. The schematic shows the incident photon with energy E_0, interacting with an outershell orbital electron that results in the ejection of the Compton electron (E_{e-}) and the simultaneous emission of a Compton scattered photon E_{sc} emerging at an angle θ of deflection. Image obtained from [84].

Since momentum and energy must be conserved, the energy of the scattered photon can be calculated from the energy of the incident photon and the angle of the scattered photon with the following formula:

$$Esc = \frac{Eo}{1+\left(\frac{Eo}{mec^2}\right)(1-cos\theta)} \qquad \text{(Eq. 3.1.1.1.3.1)}$$

where E_{sc} is the energy of the scattered photon, E_o is the incident photon energy and E_{sc} is the angle of the scattered photon [84]. The energy of the recoil electron is simply the difference between E_o and E_{sc}.

In medical imaging, with low energies (15 to 150 keV) to the scattered photon will be transferred the majority of the incident photon's energy, giving relatively high energies and tissues penetrability,

contributing to a degradation in image contrast and an increase in random noise if detected by the image sensors.

3.1.1.1.4 Attenuation

When a beam of γ-Rays or X-rays passes through absorbing materials the total number of primary photons is reduced by absorption and scattering, depending on the type of tissue. This reduction in primary signal is referred to as attenuation and it is caused by the interaction mechanisms that were described previously.

The probability that a photon has to be removed from the X-rays or γ-rays beam per unit of thickness of the material is called the linear attenuation coefficient (μ), typically expressed in cm^{-1}. The total attenuation, or linear attenuation coefficient for a given material, is expressed as the sum of each individual photon interaction:

$$\mu = \mu_{Photoelectric} + \mu_{Compton} + \mu_{Rayleigh} \quad \text{(Eq. 3.1.1.1.4.1)}$$

The attenuation of γ-Rays and X-rays in breast imaging depends on the distance the photons travel through the breast to reach the detector. Using this concept, a medical image is produced based on the intensity transmitted through the object that is detected. Thus this process can be described by the Beer-Lambert law [58]:

$$I_x = I_0 e^{-\mu x} \quad \text{(Eq. 3.1.1.1.4.2)}$$

where I_x is the beam intensity transmitted through the object of thickness x, I_0 is the original intensity, and μ is the linear attenuation coefficient.

3.1.2 X-ray Tube

An X-ray tube works as an energy converter, receiving electrical energy and turning it into two other forms of energy: X-radiation and heat. X-ray tubes are designed and constructed to maximize X-ray production and to dissipate heat as rapidly as possible. Nevertheless, about 99% of the electrical energy will be converted into heat and only 1% to X-rays via Bremstrahlung radiation, conferring only 1% efficiency to this process [84] [85].

The X-ray tube is mainly composed by two principle elements: a cathode, which provides a source of electrons, and a rotating anode that acts as a target for electrons (see figure 2.1.2.1). Depending on the tube voltages, different materials are used as anode. In mammography, since lower voltages are used, target materials such as rhodium or molybdenum are commonly used due to their suitable K-edges, with a characteristic radiation closer to the tube voltage. In DBCT, since a higher voltage is applied, that could go from 40 to 150 kV usually a tungsten anode is chosen for the X-ray tube, which operates as the electrical current flows from the cathode to the anode, resulting on X-ray emission when the electrons from the cathode collide with the anode [85].

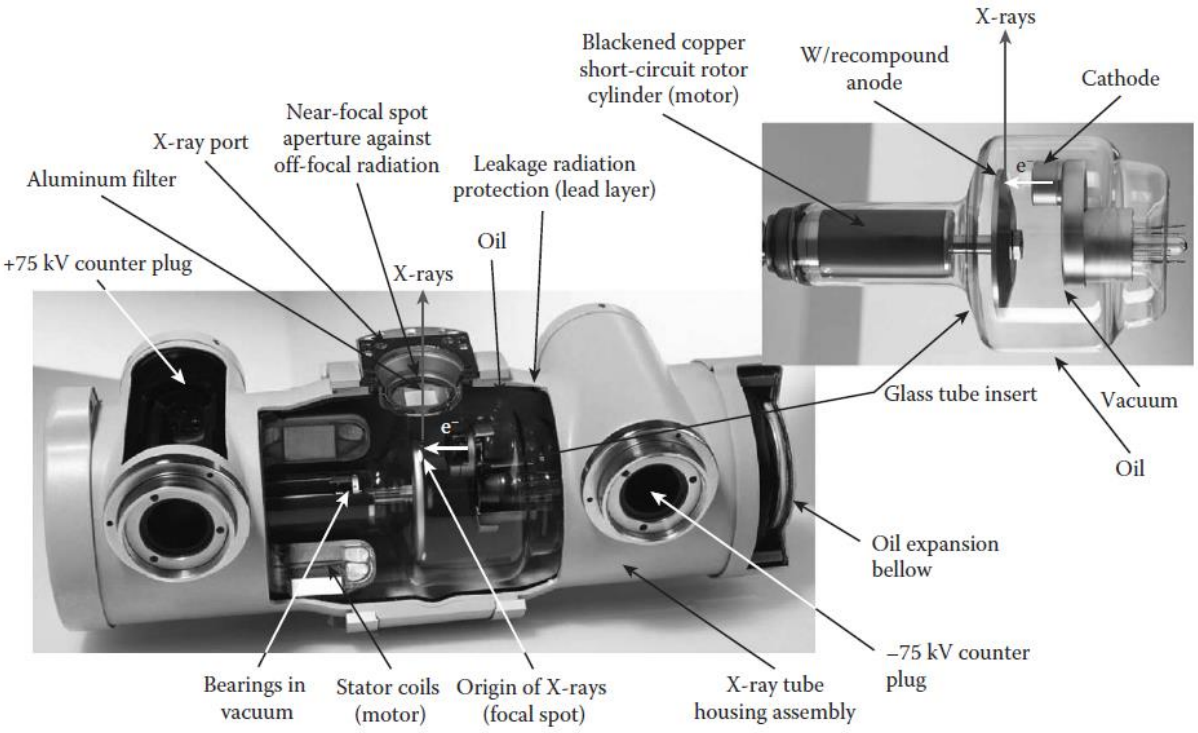

Figure 3.1.2.1. - Cut view of a X-ray tube. Image obtained from [85].

3.1.3 Flat Panel Detector

With the development of microelectronics and materials science, digital flat panel detector (FPD) has improved standard radiography since the beginning of the present millennium, not only by providing higher absorption efficiency, but also by playing an important role in problems such as lack of data storage and prompt material or the inability to perform image processing on raw data directly. FPD imaging technology has become highly relevant due to its high spatial resolution and dynamic range, providing the ability to acquire digital images rapidly, while meeting high quality detection, as well as the possibility to develop DBCT systems, with lower radiation, which could be an important exam in cancers with high prevalence in women, such as breast cancer.

All digital systems contains Analogue to Digital Converters (ADCs), which allows, by quantisation, to determine the discrete value that should be given to the signal within each pixel. The number of quantisation levels depends on the number of bits of the ADC. More bits means more accurate conversion. Measuring its accuracy is the way to verify how close the assigned digital level is to the analogue level.

In DBCT, usually a static array of detectors is used. Those detectors, schematised in figure 3.1.3.1 could be of two types: direct or indirect conversion. In indirect conversion, a X-ray scintillator is used to convert X-rays to light photons, which are subsequently transduced into a proportional electric signal using a photodiode, usually amorphous silicon (a-Si). In direct conversion, a semiconductor, typically amorphous selenium (a-Se) converts the X-rays into electrons. Afterwards, thin film transistors (TFTs) convert the electric signal into a digital X-ray image [86].

In particularly for DBCT, direct conversion is especially suited for imaging the breast due to the small energy range applied, conferring considerable higher resolution when compared to indirect conversion FPD [86].

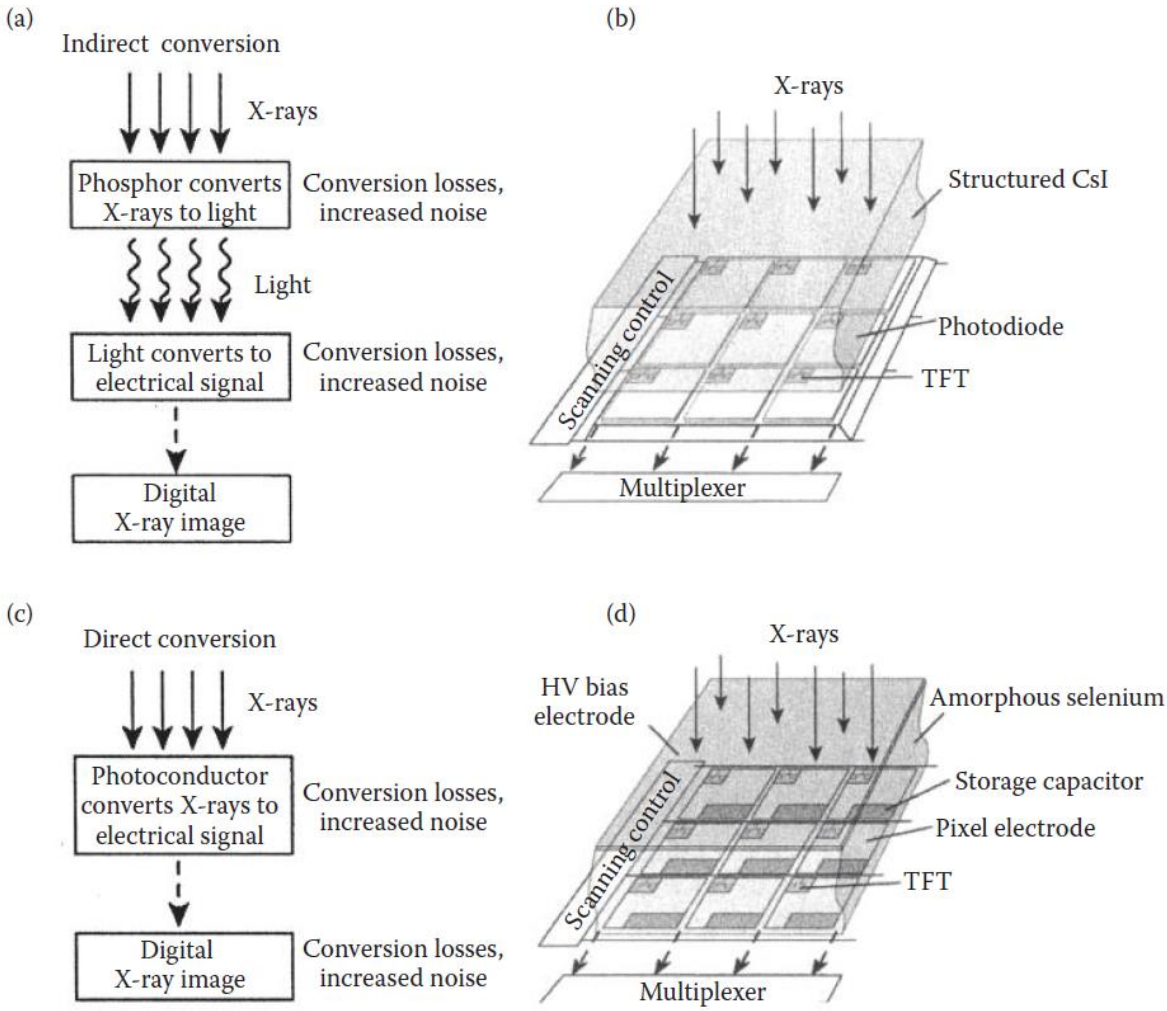

Figure 3.1.3.1 - Indirect (a,b) and direct (c,d) conversion in active matrix flat panel detectors. Image obtained from [86].

3.2 Single Photon Emission Computed Tomography

SPECT is a modality of a branch of medical imaging called emission tomography (ET). SPECT and ET are founded on an important principle called the tracer principle. Developed in the early 1900s, George de Hevesy proved that the presence of gamma radiation in radioactive compounds would not affect how they are embedded in physiological processes in an organism. The application of this principle, by combining radionuclides with biological molecules, provided the ability to track the flow, as well as the distribution of important substances inside the body. With his work, George de Hevesy was awarded the Nobel Prize in Chemistry in 1943 [87].

As the term ET suggests, SPECT results of a combination of two basic principles: imaging through the use of gamma-ray emitters, designated by the tracer principle, and 3D representation of the interior of the body, denominated as tomography.

The functional imaging provided by SPECT, with the usage of imaging agents - called radiopharmaceuticals or radiotracers - can be used to enhance the capability to detect tumours, since these radiotracers are reported to have high uptake in breast tumour cells and that uptake is not affected by breast density in this imaging exam, providing additional and complementary information to CT – which is essentially structural imaging – which could yield valuable diagnostic information [88].

The detector and the collimator are the fundamental components of any SPECT system. Together they comprise what is called the gamma camera, a design which was developed more than 50 years ago by Hal O. Anger [89].

Dedicated SPECT systems for breast imaging have been under investigation since the late 1980s. In spite of the developments with this type of systems over the last two decades, only recently was this imaging technique adopted by clinicians. The most critical reason for the reluctant and slow acceptance of this technique is the poor spatial resolution of conventional gamma cameras which causes the inability to detect sub-centimetre lesions in the breast, therefore not being able to provide a good diagnostic exam to prevent larger breast masses that could lead to mastectomies. However, recent improvements in instrumentation brought the means for the development of dedicated SPECT systems, with small detectors in close proximity to the breast, allowing to improve the spatial resolution and at the same time decrease the radiation dose in this imaging examinations [89].

As the gamma camera rotates around the object of interest, it acquires multiple projection images, which are used for reconstruction of a volumetric image of the object of interest.

SPECT has several similar physics processes to CT, such as Compton scattering which is the most important for its range of energies. The next sections will introduce the notion of radionuclide production (section 3.2.1), the main principle components of a SPECT scanner: the detector (section 3.2.2) and the collimator (section 3.2.3). Finally, a brief overview of commercial dedicated SPECT scanner is presented (section 3.2.4).

3.2.1 Radionuclide Production

For SPECT, currently only 99mTc−Sestamibi (see figure 3.2.1.2) is approved by U. S. Food and Drug Administration (U.S. FDA). This radiopharmaceutical is produced by bounding chemically two compounds: one radionuclide - in this case ^{99m}Tc – and (Miraluma®). ^{99m}Tc is an unstable radionuclide that can be a product of ^{99}Mo cyclotron bombardment or ^{99m}Tc generators. ^{99m}Tc decays to its ground state of ^{99}Tc with a half-life of 6.02 hours emitting a single photon with an energy of 140.6 keV in a γ transition as it is represented in figure 3.2.1.1 [58, 90]. The detection of photons with this energy is the fundamental principle in nuclear imaging systems like SPECT.

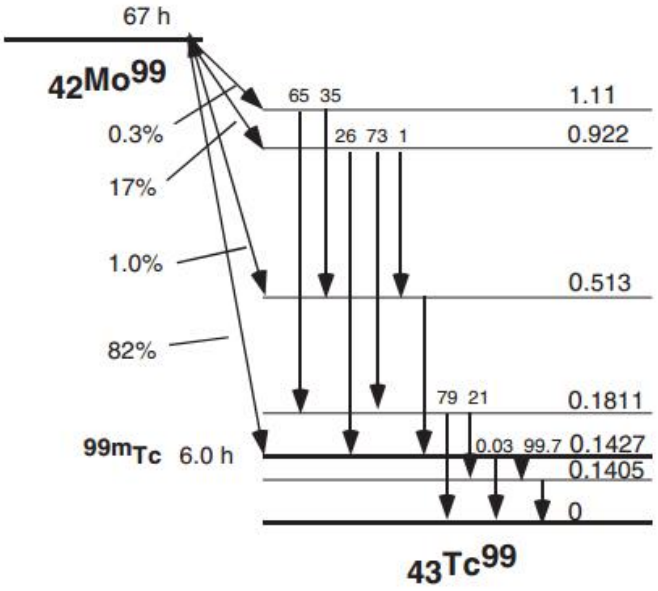

Figure 3.2.1.1. - Nuclear energy level diagram of the ^{99}Mo–^{99}Tc system for the generation and decay of ^{99m}Tc. Image obtained from [91].

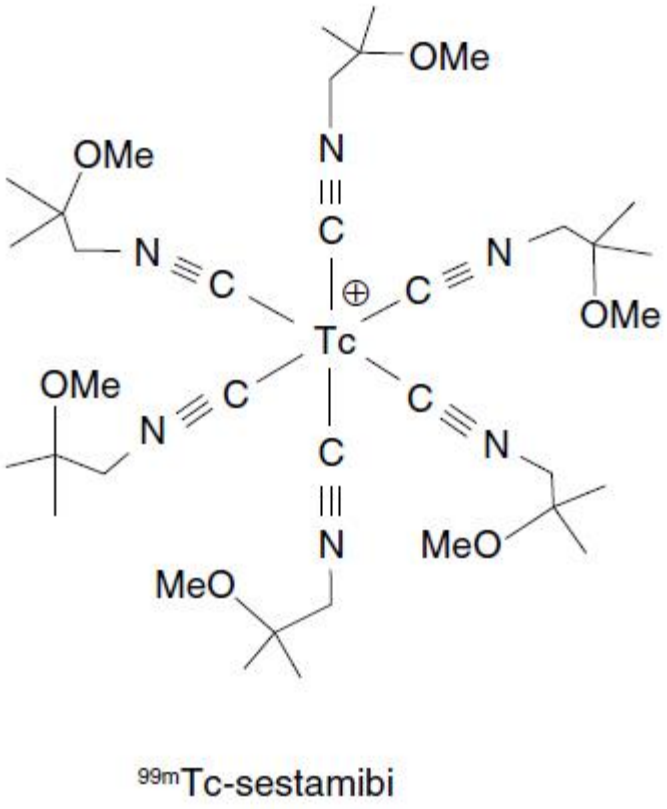

Figure 3.2.1.2. - Structure of ^{99m}TC-sestamibi. Image adapted from [91].

3.2.2 Detector

Independently of the type of system, the fundamental objective of a SPECT detector system is to convert photon with gamma-ray photons into an electrical signal. Currently, the two principal types of detector used in breast SPECT scanners are scintillating – using continuous or discrete design - and semiconductor detectors [92].

Scintillating detectors are the most common choice of detector. Sodium iodide doped with tallium (NaI(Tl)) is one the materials used in these detectors, which converts the gamma-ray photons into optical photons, when they interact with the crystal. These photons are then converted into electrical signal using either PMTs or APDs, which are much more compact than traditionally used PMTs [93, 94]. After these previous mentioned detector components, readout electronics to digitize the information, as well as amplifiers are required to be part of the detector in order for the signal to be computationally processed.

An alternative approach of compact scanners design involve discretised scintillation crystals coupled to photodetectors. Comparing with continuous design, these detectors have the ability to set the spatial resolution by the size of the crystal, since the resultant optical photons of the gamma-ray photon interaction with the scintillator are circumspect to the crystal volume where it occurred. Moreover, due to the small area of the photodetector, blur resolution and position errors are diminished. However, this design presents some disadvantages when compared with the continuous design, specifically the higher manufacturing costs and a lower sensitivity caused by the dead area between crystals. In order to detect smaller lesions, therefore diagnosing early cancer stages, good spatial linearity and high spatial

resolution are essential. Hence, a pixelated or discrete design is traditionally chosen for a breast dedicated system [95].

While scintillating gamma cameras detects the radiation indirectly, by the proportionality of photons that are produced by its scintillator crystals, semiconductor detectors directly measures an electric signal proportional to the radiation energy deposited in the detector. Due to the fact that these detectors operate with a direct conversion, they are able to provide better resolution. This fact can be attributable to the elimination of stochastic processes related with optical photons generation in the scintillators, as well as errors in the propagation and conversion to an electrical signal associated to PMTs or APDs. Cadmium Zinc Telluride (CZT) is the most thoroughly researched semiconductor for nuclear medicine imaging, providing not only better energy resolution, but also significantly smaller pixel sizes, an important characteristic for organspecific imaging like breast imaging [93, 94].

Although semiconductor detectors hold better performance, its high cost have slowed its adoption, replacing scintillation detectors in clinical practice. However, the increasing demand for organ-specific compact systems will probably escalate its production, increasing the number of units produced, which may lead to a reduction in the price of the detectors [91].

3.2.2.1 Energy Resolution

In a radionuclide imaging system energy resolution is an important measure that determines the detector's ability to distinguish interactions with the photons, especially when they are at closer range of energies, therefore being able to remove photons that have lost energy via Compton scattering or other physical phenomena. Energy resolution is usually defined in terms of the full width at half maximum (FWHM) expressed as percentage of the photopeak with mean energy (H_0):

$$E_{res} = \frac{FWHM}{H_0} \times 100 \qquad \text{(Eq. 3.2.2.1.1)}$$

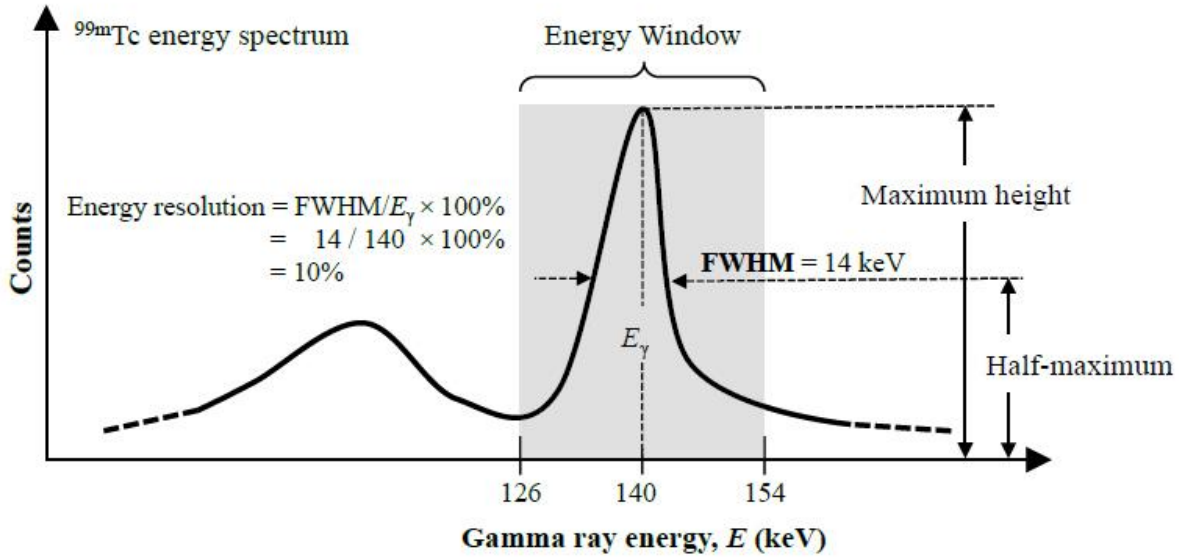

Figure 3.2.2.1.1. - Energy window that is used to select a range of acceptable photon energies. Required to compute the energy resolution of the detector. Image obtained from [96].

Energies that are within the same FWHM are considered to be unsolvable most of the times. The major contribution for the increase in the energy resolution in NaI-Tl based detectors are the statistical fluctuations of light produced in the scintillator, which will affect the number of

photoelectrons in the PMTs [97]. Less significant factors are the non-uniform light collection and the electric noise of the PMTs. Regarding semiconductor detectors, leakage current due to its finite resistivity, the determined detector Fano factor, incomplete charge carriers and the electronic noise in the amplification circuits are the causes which can increase the energy resolution [98]. Semiconductor detectors have better energy resolution when comparing to scintillating detectors, by a factor of more than two, from 9% FWHM for NaITl crystals to 3% FWHM for CZT at 140 keV, which is mainly due to its direct energy conversion [99].

3.2.2.2 Detector Efficiency

The efficiency is also an important attribute of the detector. It is defined as the number of counts in the energy window chosen for a precise radionuclide. The detector efficiency can be subdivided in intrinsic and geometric efficiency [100]. Intrinsic efficiency accounts for the photons which irradiate the surface of the detector and are transduced into proper output signals. It depends on the detector composition, thickness, energy of radiation to be detected and of the readout electronics. On the other hand, geometric efficiency is the fraction of total radiation emitted by the radionuclide that irradiates the detector surface. Therefore, geometric efficiency is heavily dependent on collimator geometric efficiency, since only the photons which cross the collimator will hit the detector. In the following subsection this topic will be addressed in more detail.

3.2.3 Collimator

The collimator is the most important component of an Anger camera in order to obtain high-quality SPECT images, given its defining role in the determination of the overall performance of the system, namely the number of detector counts and the spatial resolution. Materials with high atomic number (Z) and high density (ρ) should be able to absorb all photons travelling in different directions, blocking those photons and allowing only certain photons with specific directions, specified by the hole or aperture of the collimator. The most frequent collimator materials are lead (Z= 82, ρ = 11,33 gcm^{-3}) and tungsten (Z=74, ρ = 19,3 gcm^{-3}) [90].

3.2.3.1 Collimator geometries

Several collimators with different geometries have been developed for SPECT imaging. Factually, Anger [101] documented pinhole collimation design as the first collimator to be developed. Subsequently, parallel hole [102] and other geometries have been created [103]. In the following paragraphs an overview of the most important geometries will be provided (see figure 3.2.3.1.1).

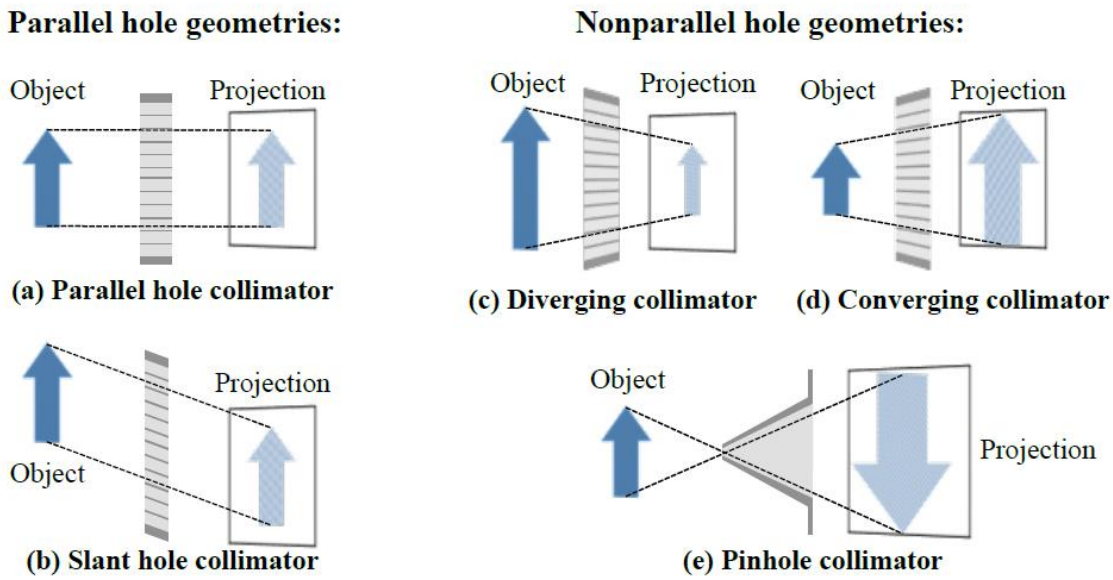

Figure 3.2.3.1.1 – Collimator geometries. Image obtained from [96].

Collimators can be classified in terms of parallel or non-parallel collimation geometries. Parallel hole and slant hole are parallel collimation geometries and diverging, converging and pinhole collimators are the non-parallel collimation geometries.

Parallel hole is the most commonly used collimation geometry. It is formed by a myriad of parallel channels or holes, conferring the projection the same size as the object, since the imaged object of interest is projected along parallel lines onto the detector.

Slant hole differ from parallel holes, because although all the apertures are parallel, they are directed at an angle to the collimator's surface, providing an oblique view, enabling the visualisation of an object which was outside of the FOV or occulted by an adjoining structure [104].

Contrary to parallel collimation geometries, non-parallel geometries give the possibility to magnify or diminish the projection's size, as well as the ability to provide a broader or narrower FOV.

Diverging collimation design, by angling the apertures outbound towards the object, provides a wider FOV, enabling the examination of a large object with a small detector, considering the smaller size of the projection compared to the size of the object of interest.

Convergent collimators, opposed to divergent collimators, possess its apertures angling inbound towards the object, conferring a magnified projection of the object of interest. The maximal magnification is obtained when the object is placed close to the focal locus, which can result in higher sensitivity or spatial resolution, compared to parallel collimation geometries. Convergent collimators can also differ in the convergence mode. In fan beam geometry the collimator holes converge to a line, acquiring a magnified projection of the object in one direction. On the other hand, in cone beam geometry is acquired a magnified projection in both direction, since the apertures converge to a point [90].

Sharing beam characteristics with convergent collimators, pinhole collimator geometry design confers magnification of the object of interest with a single aperture. Maximum magnification results when the aperture is closest to the object and decreases as the pinhole is moved further away. These properties shaped pinhole collimators to be very successful in small animal imaging [105].

The collimator design is much diversified and should be paired to the imaging problem to be addressed. In the next chapter a succinct approach to the performance of the collimator will be discussed.

3.2.3.2 Collimator performance

A precise evaluation of a complex function labelled as the point spread function or point source response function (PSRF) is required to describe the collimator performance. Used in various contexts, from optics, astronomical imaging and another imaging techniques, it describes the image elaborated by a point source as a function of its position and the location in the image plane.

Suggested by Anger [102], the PSRF theory has been applied for describing the response of imaging systems constituted by a parallel hole collimator with a continuous scintillation crystal [106]. Nonetheless, when analysing performance in pixelated systems, the discrete readout scheme must be taken into account, contrasting with the analogical readout of continuous crystals systems. To address this problematic, Wieczoreck and Goedicke [107] proposed a different alternative to evaluate pixelated detectors, based on PSRF, which was nominated as single pixel response function (SPRF).

Since both PSRF and SPRF theories are too complex, making collimator comparisons very challenging, most researchers chose to use only sensitivity and spatial resolution as they access the most important effects of the response function [106].

Geometric efficiency or collimator sensitivity is described as the portion of the emitted photons that cross the collimator and hit the detector surface. For the SPRF theory this parameter is calculated by multiplying the average area of one pixel by the portion of gamma-radiation that reaches one detector pixel and dividing this previous value by the voxel area, in other words, the area of the object plane correspondent to one detector pixel, as described in figure 3.2.3.2.1. The combination of these three previously enumerated factors, provides the bases for calculating the geometric efficiency of a parallel hole collimator using septal thickness t, hole diameter (parallel-to-parallel side distance) d, detector pixel pitch $p = d + t$, source-collimator distance z, collimator thickness L and source-detector $z' = z + L$ using the given formula:

$$E_{parallel} = \frac{d^2}{4\pi L^2}\frac{d^2}{p^2} \qquad \text{(Eq. 3.2.3.2.1)}$$

Although the equation 2.2.3.2.1 have been analytically calculated and have not taken into account the septal penetration effects, it clearly states that the collimator sensitivity is not affected by the source position within the camera's FOV [106]. As matter of fact, it is the sole collimation geometry which provides a homogeneous efficiency, independently of the source-collimator distance value [97].

Spatial resolution is usually described as the smallest distance at which two point sources can be distinguished. Considering the relation of the spatial resolution, R, to the distance of the imaging plane to the object plane, its value is calculated as the FWHM of the SPRF for a point source in the object plane, as shown in figure 2.2.3.2.1. Spatial resolution is equivalent to horizontal central part of the SPRF, with width d, and the width of one slope of length dz/L, thus coming to the following formula [97]:

$$R_{parallel} = d\frac{z'}{L} \qquad \text{(Eq. 3.2.3.2.2)}$$

where d is width, z' the source-detector distance and L the collimator thickness.

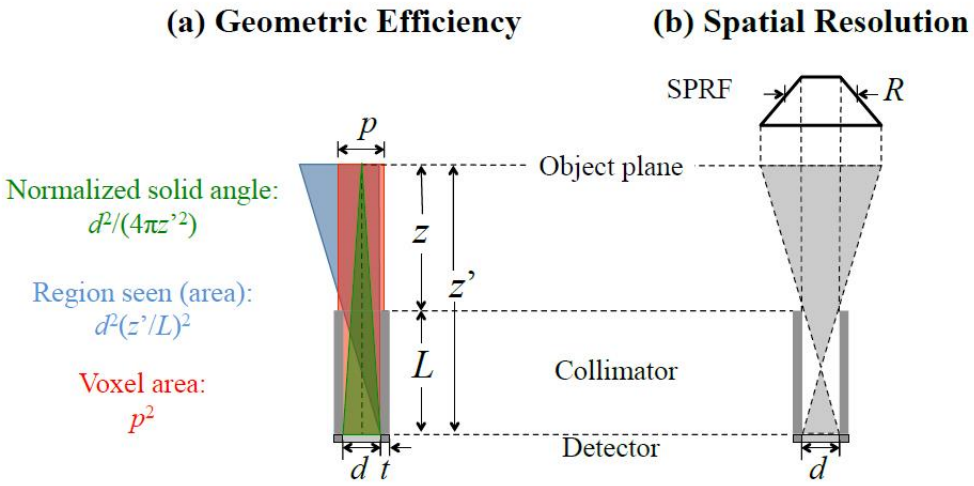

Figure 3.2.3.2.1. - Collimator performance. Image obtained from [96].

As the value of R decreases, an increasingly better collimator spatial resolution is therefore obtained, yielding better quality images, by improving contrast and spatial detail of the final image. With a fixed source-detector distance z', the sole approach to improve spatial resolution is by enlarging the collimator thickness L and diminishing the hole diameter d. Nonetheless, while increasing the spatial resolution, geometric efficiency decreases, leading to trade-off situation, which is normally expressed as the proportionality [106]:

$$E_{parallel} \propto (R_{parallel})^2 \qquad \text{(Eq. 3.2.3.2.3)}$$

3.2.4 Commercial Breast SPECT scanners

Despite the intensive research in the development of dedicated breast SPECT systems, solely three types of system are commercially accessible (see table 2.2.4.1) [91].

In the breast specific gamma imaging (BSGI) system Dilon 6800 (Dilon Technologies, Newport News, VA, USA) the breast is slightly compressed between a single detector head with NaI scintilattors and PMTs and a compression paddle to minimise motion artifacts during exam acquisitions. A patient study from R. F. Brem et. al [108] showed that this particular system granted enhanced sensitivity for sub-centimeter and non-palpable lesions, when compared to scintimammography using an unspecialised gamma camera.

The Discovery NM750b (GE Healthcare, Milwaukee, WI) and the LumaGEM 3200s (Gamma Medica, Inc., Northridge, CA), since are dedicated CZT-based detectors, they are also designed as molecular breast imaging (MBI) systems. Both systems operate in a similar manner, using a dual head detector, the breast is gently compressed not only to reduce patient motion, but also to reduce breast thickness. The disposition of this system certifies that no tumour mass is more distant than half of the breast thickness from one of the two detector heads. A study from C. B. Hruska et. al [99] showed improved sensitivity of sub-centimetre masses detection, when compared to a single detector head. Similarly, it has also been stated with several studies that the sensitivity in BSGI systems improves when using a dual head configuration, improving lesion detection [91].

SPEM system	System geometry	Scintillation materials	Photodetector	Pixel size (mm^2)	Detector size (cm)
Dilon 6800 (BSGI)	One head	NaI	PSPMT	3×3	20×15
Discovery NM750b (MBI)	Dual head	-	CZT	2.5×2.5	20×20
LumaGem 3200s (MBI)	Dual head	-	CZT	1.6×1.6	20×16

Table 3.2.4.1 - Specifications of the commercial dedicated SPECT scanners [110-112]. Table obtained from [96].

Although mammography is the gold standard in breast imaging and currently the only imaging modality used in screening, it is expected to see complementary imaging exams in screening in the next few years.

Recent clinical studies completed by O'Connor's research group, exhibited the capability of MBI systems to detect lesions that were not signalised in mammography exams. This situation is even more critical when mammography performance is severely compromised when imaging dense breasts, therefore the current clinical trends goes toward nuclear imaging, which is not affected by breast density, more specifically dedicated SPECT, which at a decreased radiation dose showed a good performance as screening procedure [109,113-115].

Despite the fact that chest wall and axilla cannot be visualised in these commercial systems [91], not only dedicated SPECT systems demonstrated comparable sensitivity to MRI at fraction of the cost, but also can provide 2D information, helping in the process of comparison of resultant images with mammograms [116].

3.3 Tomographic Image Reconstruction

In tomographic imaging, with techniques such as SPECT and CT, tens to hundreds of projections at different angles are acquired around the object of interest. Each projection represents the line integral for a specific direction of the transmitted intensity or emitted radiotracer activity, for CT and SPECT, respectively, as represented in figure 3.3.1.

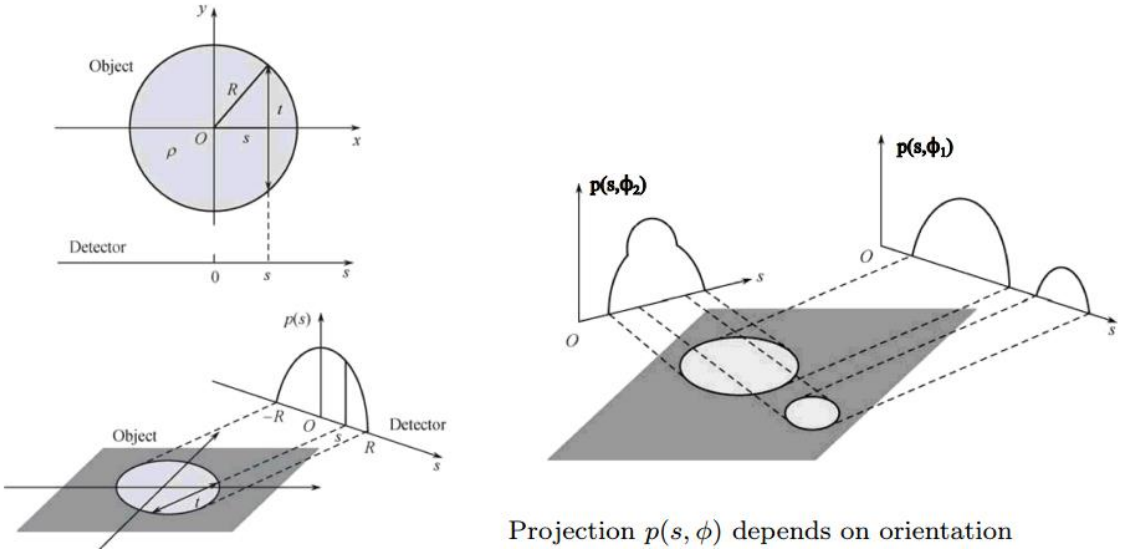

Figure 3.3.1. - Two different angle projections. Image obtained from [117].

Reconstruction is a crucial point in medical imaging. It is dealt as an inversion problem and it has a major importance in order to produce good quality images. Using the acquired projections, a 3D

volumetric image representation of the object of interest is created by applying mathematical algorithms. The two previously mentioned tomographic techniques may have reconstruction algorithms in common, but while in CT the procedure involves reconstruction of the attenuation coefficients from the projection data, in SPECT the activity concentration of the radiotracer is what must be modelled. These reconstruction methods, by introducing the notion of depth with 3D visualization, improve the contrast due to the removal of overlapping structures, therefore providing better spatial resolution and more precise quantification of radiotracer activity in SPECT and a complete attenuation coefficient map in CT when compared to conventional 2D radiographs [58].

These reconstruction algorithms have modelling assumptions that are different for each imaging modality. In CT, the X-Rays beams are assumed as traveling along straight lines, with a monoenergetic source and that each type of material has a characteristic linear attenuation coefficient for a specific energy of X-Rays, according to Beer's law:

$$\int_I \mu ds = -\ln\left(\frac{I}{I_0}\right) \quad \text{(Eq. 3.3.1)}$$

where μ is the linear attenuation coefficient, s is the arc length and I and I_0 are the X-ray intensity after and before interacting with matter [117]

In SPECT, a continuous and complete sampling of the data and the absence of physical effects such as attenuation, scatter, radiotracer half-life, collimator blurring and that every photon which hits the detector is absorbed are the assumptions required for modelling the activity distribution along a certain line of response (LOR):

$$E[p(\lambda)] = \int_\lambda f(x,y,z)dxdydz \quad \text{(Eq. 3.3.2)}$$

where $p(\lambda)$ is the projection along the LOR λ and $f(x,y,z)$ is the radiotracer distribution throughout the volume of interest [117].

The central concept in which image reconstruction is based is that the system can be described as:

$$y = S(x) + noise \quad \text{(Eq. 3.3.3)}$$

where y are the measurements i.e. the projections, $S(x)$ is the system operator, and x is the activity in case of SPECT and the attenuation coefficients in case of CT. The noise will not be considered in this dissertation.

Usually the system operator is approximated to a system matrix, which is the probability of the emission - for SPECT – and attenuation – for CT – in voxel i is reflected by the measurement at the detector in j.

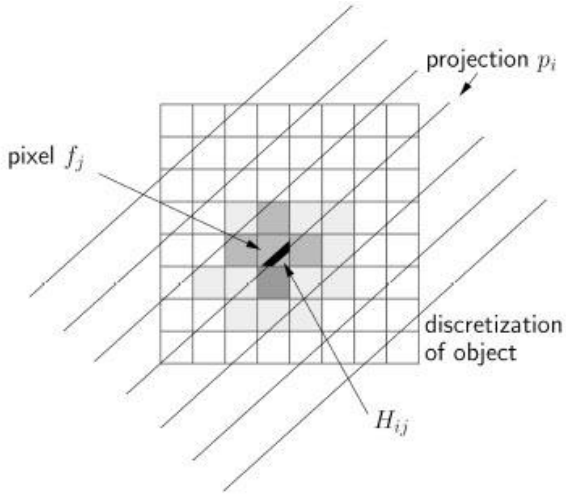

Figure 3.3.2 – Discretisation of each projection contribution to the value for a certain pixel. Image obtained from [117].

With a linear approximation of $S(x)$, since y_i is known, x_i can be calculated by inverting the equation:

$$y = Ax \Leftrightarrow x = A^{-1}y \qquad \text{(Eq. 3.3.4)}$$

using analytical or iterative methods.

The reconstruction methods used can be subdivided in analytical and iterative algorithms. Filtered backprojection (FBP) is the most commonly used reconstruction algorithm in CT, being able to provide radiologists images in a matter of seconds [117]. However, the inabilility for modelling assumptions for FBP, alongside with an increasing computing power, led to an increasing interest in the development of new iterative methods that could incorporate prior knowledge, including object constraints, system geometry and detector response, combined with the ability to modulate noise or even account for physical phenomena such as beam hardening [117].

The following sections 3.3.1 and 3.3.2 will present with more detail a series of analytical and iterative techniques.

3.3.1 Analytical Algorithms

Filtered backprojetion is the most widely used analytical algorithm to solve the inversion problem of image reconstruction. It takes into account the relation between the Radon transform and the Fourier transform in the following equation:

$$F\{p(s)\} = P(w) = \frac{1}{\sqrt{2\pi}} \int_{-\infty}^{\infty} p(s) e^{-iws} ds \qquad \text{(Eq. 3.3.1.1)}$$

Afterwards this information is incorporated in the central slice theorem, which states that the measured projection data is related to the 2D Fourier transform of the object cross sections:

$$F_1\{p(s, \phi')\} = F_2\{f(x,y)\}_{|\phi=\phi'} \qquad \text{(Eq. 3.3.1.2)}$$

Basing on this relationship the image $f(x,y)$ can therefore be obtained via the inverse Fourier Transform, in a process described in figure 2.3.1.1 using this equation:

$$f(x,y) = \int_0^{\pi} d\phi \left[\int_{-\infty}^{\infty} dw |w| P(w) e^{2\pi i w s} \right]_{s=x\cos\phi + y\sin\phi} \quad \text{(Eq. 3.3.1.3)}$$

where P(w) is the Fourier Transform of projection $p(s,\phi)$, which is multiplied by the frequency filter $|w|$, which is usually a ramp filter. Afterwards, this product is inverted backprojecting the filtered projection. The last step is a final summation over all filtered projections, providing a 3D reconstructed image of the object.

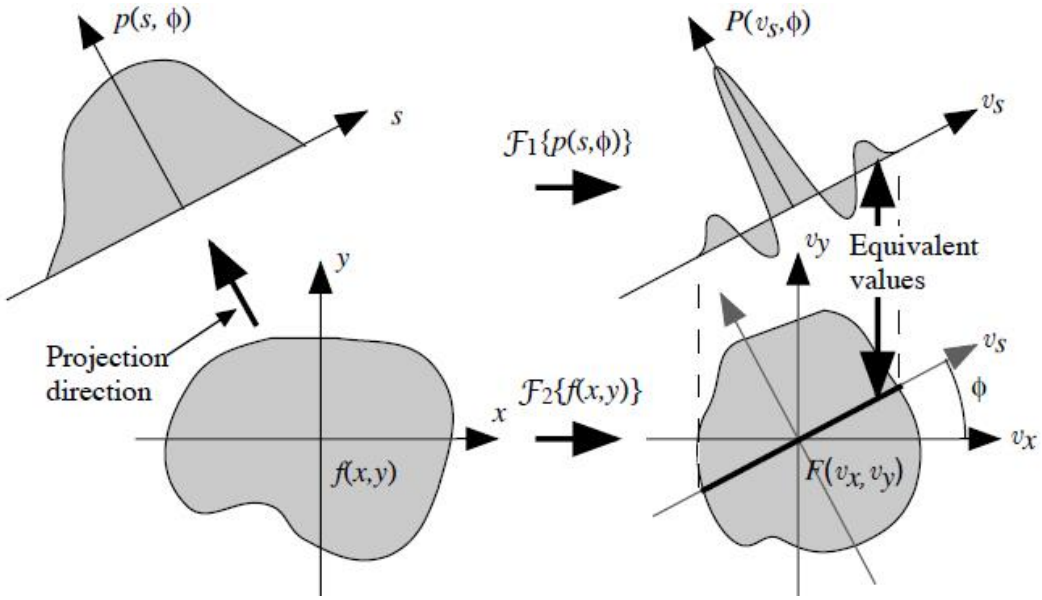

Figure 3.3.1.1. – Projection transformations [117]

The first pratical algorithm for CBCT, which is the CT technique used in this work is the Feldkamp-Davis-Kress algorithm, which was formulated in 1984 and provided the ability to reconstruct a 3D image with projections acquired from a circular source trajectory with a planar detector [117].

The next section will concern an alternative to analytical algorithms – iterative reconstruction algorithms – which provide a more versatile, but less time efficient approach when compared to analytical algorithms.

3.3.2 – Iterative Algorithms

In the most recent years, the challenges presented by CBCT and multi-slice helical CT towards the limits of FBP led to an increasing interest in the development of iterative methods that could overcome FBP limitations.

With an increasingly cheaper computation power to perform iterative techniques, the ability to incorporate prior knowledge, including system geometry, object constraints, detector response as well as modulate noise sustained this interest in the development of these algorithms. It is also worth mentioning the capability to incorporate in the model physical phenomena, such as beam hardening or a polyenergetic acquisition, therefore enhancing the accuracy of the reconstruction. On the other hand, the main disadvantage of these iterative techniques is the high computation time [117,118].

The principle of iterative algorithms is to find an optimal solution by successive estimates. It compares the current estimation to a measured projection. This result is used to modify to improve the current estimation until the point of convergence.

The way that the estimated projections are obtained differ for each one of these algorithms, but in general can be described by following steps:

- make a first arbitrary estimation;
- project the estimation into the contiguous projections;
- compare the projection of the estimations with the measured projections;
- evaluate if the stopping criteria is satisfied;
- update the estimation if the criteria is not satisfied;
- repeat the whole process.

The following paragraphs will merely ilustrate the principal methods applied in CT and SPECT. Since the main purpose of this work was to discuss the feasibility of this system, reconstruction was not evaluated and the FBP and MLEM algorithm were the only algorithms applied to reconstruct 3D image for CT and SPECT, respectively.

ART was first proposed in 1970 by Gordon et al. Conceptually simpler and more adaptable to missing data than FBP, it assumes that the cross-sections of the object to be imaged consist of arrays of unknowns. Thus, the reconstruction problem can enunciated as a system of linear equations, with an iterative method being applied to solve the following equation:

$$m^{(k+1)} = m^{(k)} + \lambda^{(k)} \frac{b_i - \langle r_i, m^{(k)} \rangle}{\langle r_i, r_i \rangle} r_i \qquad \text{(Eq. 3.3.2.1)}$$

where the term λ, which is called relaxation, is commonly introduced in order to reduce the noise and accelerate the process.

The principle algorithm used in ART is the Kaczmarz method which was formulated in 1937.

Despite its advantages towards FPB, the size of these system equations and the lower accuracy and the fact that, as FBP, doesn't account for physical phenomena, such as beam hardening are the main disadvantages of ART techniques.

On the other hand, Simultaneous Iterative Reconstruction Technique (SIRT) allow to introduce more detailed information, regarding not only the system geometry, object response or detector response, but also physical phenomena such as polyenergetic sources or beam hardening. Using algorithms which are based on modelling assumptions that incorporate the stochastic nature of physical measurements, combined with statistical methods provide better results when compared to the reconstruction techniques previously enumerated.

This technique is most widely used in CT, but despite having several advantages towards ART or FBP, the reconstructions can be easily contaminated by noise, usually requiring a regularisation term. The principal disadvantage is the computation requirements that are longer than other methods.

In SPECT MLEM is the most commonly used technique to reconstruct 3D volumetric from projections. By assuming a random Poisson distribution of the radiotracer's activity the basic principle of this method is to choose an image x that maximises the probability of producing the original image. Specifically, for MLEM the log-likehood is what is maximised:

$$\log(L(x)) = \log(p(y|x) = \log(\prod_i p(y_i|x)) = log\left(\prod_i \frac{e^{-Ai \cdot x}(A_i \cdot x)^{y_i}}{y_i!}\right) \qquad \text{(Eq. 3.3.2.2)}$$

Briefly, the ML-EM algorithm starting with an initial guess $x_i(0)$, simulates measurements from estimate, which are then compared with actual measurements used to improve the image estimate until a certain convergence criteria or number of iterations are completed according to the following equation:

$$x_i^{(n+1)} = x_i^{(n)} \cdot \frac{1}{\sum_j A_{ij}} \cdot \sum_j A_{ij} \frac{y_j}{\sum_k A_{kj} x_k^{(n)}} \quad \text{(Eq. 3.3.2.3)}$$

OSEM, firstly proposed by Hudson and Larkin in 1994 [119] is a variation of the ML-EM algorithm. It allows to accelerate the reconstruction process by dividing the data into ordered blocks and promoting a faster convergence to the optimal result.

Due to an increased computing capability, every year are proposed new techniques, being amongst them not only completely new techniques, but also hybrid techniques than combine already existing techniques.

3.4 Monte Carlo Simulations

MC simulations are computational techniques that attempt to model several problems of different domains of exact sciences, being able to describe completely different situations such as radiation interactions with matter and stock behaviour.

Based on random variable sampling which use sequences of random numbers, MC simulations are able to solve problems by repeating the process until a certain criteria or precision is obtained. This method is particularly well suited for statistical problems, but can also be used in problems where the exact solution is difficult or impossible to obtain.

The exponential growth in computation power led to the development of newly and sophisticated MC methods covering a broader spectre of applications, even replacing or being seen as a serious alternative to well established analytical methods [120].

Historically, its origin dates back to the XVIII century when Georges Lòuis Leclerc, Buffon's earl, proposed a method to calculate π using a stochastic experiment, known as Buffon's needle. The name Monte Carlo would have been suggested by Stanislaw Ulam, in a clear reference to the type of game practiced at the famous Casino of the city of Monte Carlo in Monaco in the late 1940s by Stanislaw Ulam, while he was working on nuclear weapons projects at the Los Alamos National Laboratory [121].

Given the stochastic nature of radiation emission, transport and detection process, MC are used in different fields of medical physics such as radiotherapy, radiation protection and nuclear medicine. In the early 1960s, H.O. Anger was the first to use MC methods in nuclear medicine to simulate the physical response of his new scintillation camera. Nowadays, this simulation method represents an important role in research, design and optimization of new or installed imaging systems, development of image reconstruction and correction techniques or even to perform quality assurance of commercially installed imaging systems.

In general, MC methods consists in constructing a model of an imaging system, as realistic as possible, and simulate physical interactions with that system. Using pseudo-random number generators (PRNG) and models of radiation transport processes MC simulations are carried in order to determine the probability of certain particles to travel through given materials. Therefore, MC methods are able to simulate physical processes and the response of the imaging systems providing several different applications and studies that, according to Buvat [120] could be subdivided in 5 different levels:

- Studying system design;
- Evaluate the accuracy of quantitative methods;
- Analysing the contribution of different quantitation topics (characterise the relative importance of attenuation, scattering and partial volume effect);
- Designing correction techniques for quantification;
- Performing receiver operating characteristic (ROC) analysis.

One of the main concept behind MC methods is the use of exponential attenuation law, which states that photons part of a monochromatic beam have a certain probability of interaction per length unit described by:

$$\int_0^\infty \exp(-\mu \cdot x)\, dx = \frac{1}{\mu} \quad \text{(Eq. 3.4.1)}$$

This allows to know, using a PRNG for the exponential distribution, the total photon path length:

$$s = -\frac{1}{\mu}\log(\xi) \quad \text{(Eq. 3.4.2)}$$

where ξ ~U(0,1) [120].

3.4.1 Pseudo-Random Number Generators

MC simulation is based on the use of pseudo-random number generators to generate different probability distributions, since real random numbers are hard to generate and its quality depends on several experimental factors which are difficult to control. The more efficient way of generating random numbers is by using computer algorithms. Although the numbers are independent between each other, all list of numbers can be predicted if the algorithm and its seed are known make it therefore a list of pseudo-random numbers [120].

There are several different PRNGs. The most widely used is the linear congruential random number generator (LCRNG), but there are others such as the Lagged Fibonnaci Random Number Generator (LFRNG), which is increasingly popular, especially with extremely long periods where they are generally faster than LCRNG and have excellent statistical properties [120].

3.4.2 Variation Reduction Techniques

To optimise the use of PRNG and reduce MC simulation variation reduction techniques can be used. There are several different techniques that can be applied, but its application must be extremely careful, because when misapplied can easily lead to erroneous results. The golden rule for MC simulation is to avoid unnecessary calculations.

One of the most important techniques is the universally used energy cuts, which introduces energy limits to follow primary or secondary particles. When correctly applied the simulation time can be reduced up to a factor of 10.

Finite range rejection is a technique that consists in stopping the particle transportation provided the fact that it has a low probability to hit the region of interest. However, the user should be wary that its application might introduce bias by not producing secondary particles that could be important to the MC simulation.

Symmetries and geometric cuts are also an important source of reduction of simulation time. Especially when dealing with similar or symmetric components the simulation can be reduced by simulating solely part of the structure, replicating the results to similar parts of the systems.

Particle multiplication is a technique specially used when dealing with bremsstrahlung radiation generated photons and as the name suggests, it multiplies the probability of a certain particle to interact with the region of interest. On the contrary, the technique of russian roulette retains only a percentage of the particles and annihilates the other.

Finally, forced interaction can also be used for MC simulations when a significate part of the radiation does not interact with the system, increasing the simulation time and diminishing the primary

particle statistics. The main concept is to compel the primary particles to interact with the volume of interest, therefore increasing the interaction probability [122].

3.4.3. Monte Carlo Codes used in Medical Imaging

Currently, the existing MC codes which are used to simulate medical imaging systems can be subdivided in general purpose codes, such as MCNP [123], Geant4 [124] or PENELOPE [125] or dedicated codes like SimSET [126] and GATE [127].

General purpose codes, which were initially developed to address the simulation of particle transportation in a broad range of areas, have been proven feasible and presents several advantages. Used by a large community of researchers these codes are generally well documented, usually maintained in the public domain, benefiting of the collaboration environment of open-source concept, providing normally extensively examined codes, regular releases, which make a long-term existence of these codes to be expected. However, since they are designed to address numerous situations, the size of the code is larger than necessary for most situations, having not only irrelevant features for specific simulations, but also could require a time consuming process to learn how the programs work. In addition, since the codes are not specially designed for any imaging system, intensive programming is therefore needed to perform new simulations [120, 128].

On the other hand, specific MC codes are designed for one or a restrict set of medical imaging systems. Unlike general purpose, these codes are relatively easy to learn and implement, since they are confined to model a smaller set of parameters and have less features when compared to general purpose codes. On the other hand, the smaller community must be taken into account, forasmuch as they cannot provide the same capability to examine the code, as well as further development in order to maintain regular releases, making its long term existence to be uncertain. In addition to this disadvantage, the specificity of these codes might not present the user with the required flexibility to adapt the code not only to a new application, but also even to keep up with the developments in the techniques they should model.

GATE is a MC simulation package based on GEANT4 dedicated to nuclear applications, which was initially developed in 2001, combining well validated physics models, the ability to design complicated geometry and powerful visualisation and rendering tools.

Using a dedicated macro language, eliminating the need for an extensive C++ programming that would be required if using GEANT4 by itself, a community that has been steadily increasing is allowing GATE to provide a MC code that ensures reliability and long-term support and flexible enough to model most of the imaging systems [127].

GATE had a tremendous impact on the research community with thousands of active users and with a recognition through the main article related to GATE by the Editorial Board and International Advisory Boards of the prestigious journal Physics in Medicine and Biology as one of the most 25 important works published in 60 years' existence of the journal [127].

The introduction of CT modelling in GATE version 6.1 and the ability to model multiple imaging systems from GATE version 7.1, determined the choice of this program to design a model encapsulated in a single program, which will be presented in this dissertation.

4 Experimental Methods

4.1 Simulation Framework

To perform the simulations a computer cluster with 4 executions machines, each one with: 8 CPUs (Intel® Xeon® CPU E5345@2.33 GHz), 12 GB of RAM and CentOS (release 5.11) operating system using a Sun Grid Engine (SGE) software system was used. In figure 4.1.1 a flowchart illustrates how this system works to perform MC simulations.

In order to extract the maximum of its computer power, several commands were required to perform a complete simulation. First, the SGE commands need to be added to the path by using:

```
source PATH_TO/sge/default/common/settings.sh
```

Afterwards, the Gate environment variables are added to path as well as using a similar command:

```
source PATH_TO/Gate/env_gate.sh
```

Then, several files are created using the command:

```
PATH_TO/Gate/bin/Linux-g++/gjs -numberofsplits 10 -clusterplatform
sge MainMacro.mac
```

allowing to split the simulation up to the number of processors available for computation at the cluster machine. For illustration purposes, in the above command the MC simulation was split into 10 different macro files. Afterwards, these were submitted to the cluster by executing a .submit file, generated by the previous command, which automatically assigns each macro to a different processor of the cluster.

Finally, a script was written in python to combine all the output files in a single file. By using regular expressions, the script took advantage of the fact that each output file was named by adding a sequential number starting in 1, allowing the user to define the name of the output file which combined the information of all the cluster output files:

```
import os
import re
gen_root_name = raw_input("Please enter the beginning of your
generated root files: ")
final_root_name = raw_input("Please enter the desired name of your
merged root file(without \".root\"): ")
my_regex = re.escape(gen_root_name)
name_total = ""
for file in os.listdir("./"):
    if file.endswith(".root"):
        if re.search( my_regex, file, re.IGNORECASE):
         name_file = str(file) + " "
         name_total = name_total + name_file
os.system("hadd " + final_root_name + ".root " + name_total)
```

The following section will briefly introduce how GATE implements MC simulations, with a

detailed description of every step required for the development of the macro simulation files.

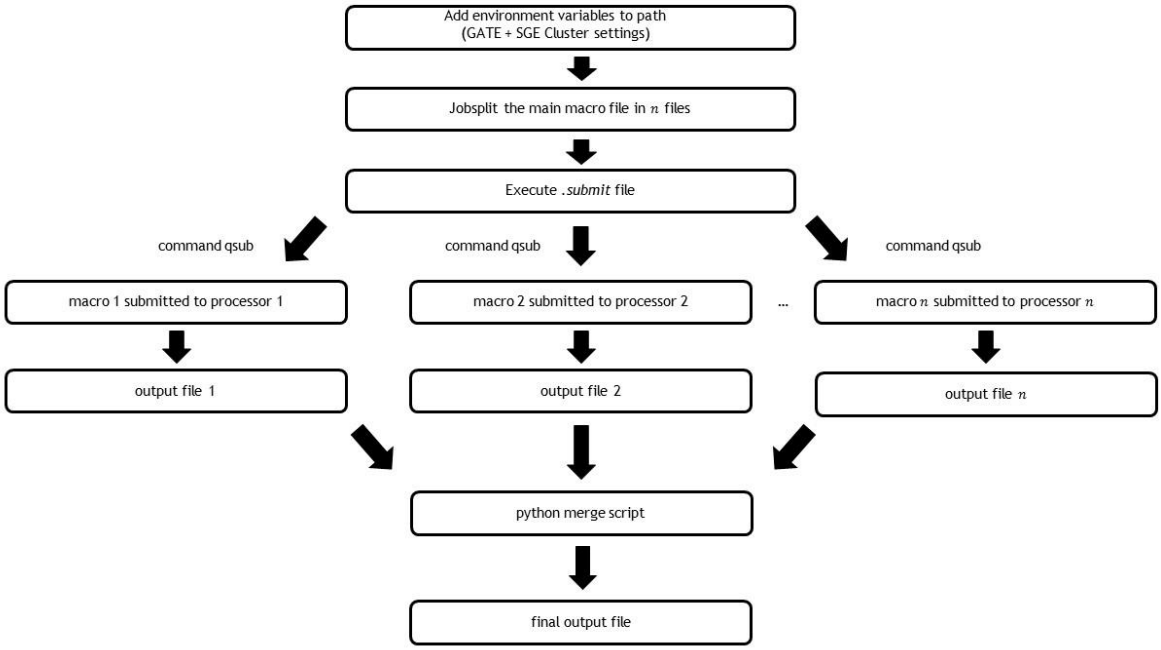

Figure 4.1.1. - Simulation Framework.

4.2 Monte Carlo Simulations

To perform the MC simulations GATE version 7.1 was used. This program combines the advantages of the Geant4 simulation toolkit well-validated physics models, sophisticated geometry description, and powerful visualization and 3D rendering tools with original features specific to emission tomography.

GATE consists in several hundred C++ classes. The core layer of C++ classes created by mechanisms used to manage time, geometry, and radioactive sources is close to the Geant4 kernel. The implementation of user classes from the core layer classes, such as geometries definition or operations over volumes - such as rotations and translations - is called the application layer. Finally, a dedicated scripting mechanism - the macro language - that extends the native command interpreter of GEANT4 substitutes the requirement for C++ programming, allowing to perform and control MC simulations of realistic setups using simple scripts.

A schematic of the architecture of GATE is presented below [129, 127]:

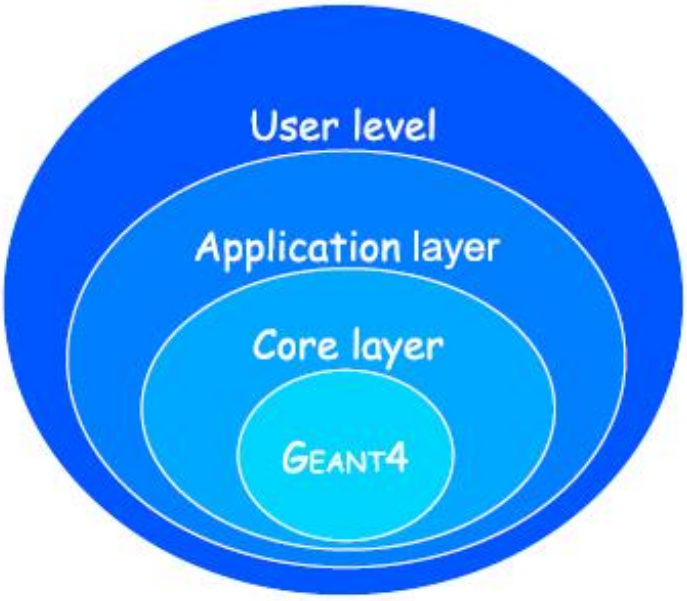

Figure 4.2.1. - Structure of GATE. Image obtained from [130].

For each Gate simulation there are eight main steps which need to be performed:

1. define the scanner geometry;
2. define the phantom geometry;
3. set up the physics processes;
4. initialise the simulation;
5. set up the detector model;
6. define the source(s);
7. specify the data output format;
8. start the acquisition.

Steps 1) to 4) concern the initialisation of the simulation (*PreInit* > *mode*). The following four steps are performed in the *IDLE*> *mode*, where the geometry can no longer be changed [130].

All volumes are encapsulated in the so called *world* volume, which is simply a box with x, y and z dimensions set by the user. Afterwards, the definition of the scanner and phantom geometry proceed in a similar way, where the dimensions and shapes are specified. The main difference from the *world* definition is that the materials of each volume are defined from a file usually called *GateMaterials.db*. After its creation, the volumes can be repeated in different ways and with different placements, according to *translation*, *rotation* and *alignment*.

After the description of the volumes and corresponding sensitive detectors, the specification of which interaction processes are to be included in the simulation is needed. In order to do that, not only the types of particles to be transported and the physics processes to be taken into account, but also the production cuts must be specified by the user. GATE uses the GEANT4 models for physical processes. The user has to choose among these processes for each particle, depending if it is for photons, electrons or electron-positron annihilation. For each type of interaction, the user can choose between two models or ignore the interaction completely.

After the initialisation of the simulation, as referred above, the user has to set up the digitizer, which accounts for all the hits information regarding time, position and energy of each hit, Then, followed by the source definition according to the type of emission. Finally, the user has to define the output formats and start the acquisition.

In order to execute the different MC simulations, comprehensive scripts using the GATE macro language were designed. The architecture used in all simulations contemplated a main macro, which in turn would call every part that were previously described in this chapter sequentially as illustrate in figure 4.2.2.

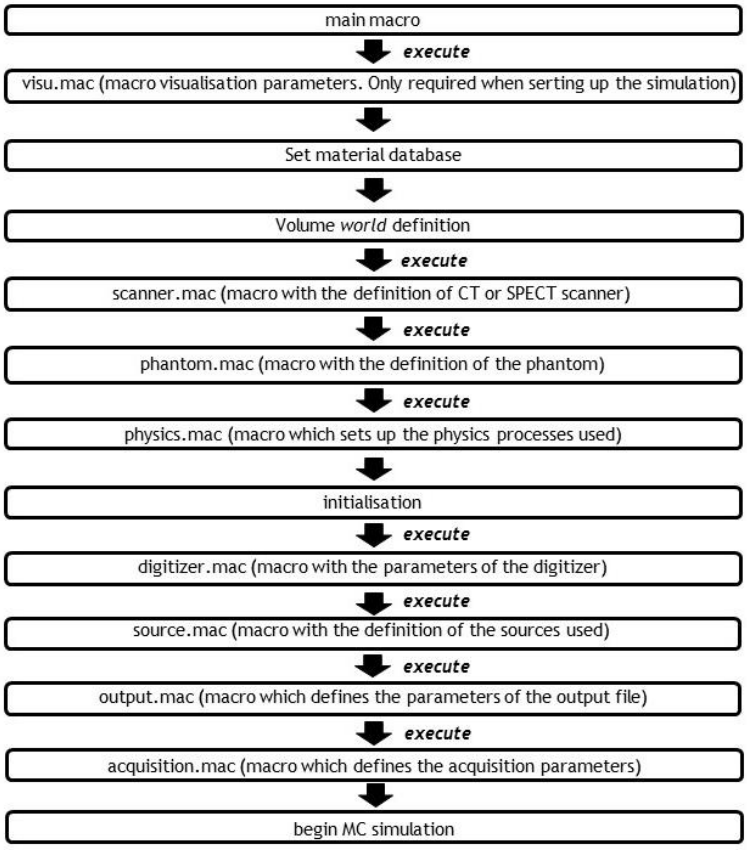

Figure 4.2.2 - GATE Macro Simulation Flowchart.

Using Gate version 7.1, the simulations were conducted on a computer cluster with 4 executions machines, each one with: 8 CPU's (Intel® Xeon® CPU E5345 @2.33 GHz), 12 GB of RAM and CentOS (release 5.11) operating system.

In the following subsections will be described with more detail the steps taken for each simulation starting with the phantom geometry, which is common to both systems.

4.2.1 Phantom Geometry Definition

For both CT and SPECT simulations the same phantom was used. What differed between simulations was only the number of lesions used in SPECT and CT.

To simplify the simulation a cylindrical phantom was chosen with a 35 mm radius and 150 mm height, defining its material as breast tissue using the composition described in [131].

```
/gate/world/daughters/name breast_phantom
/gate/world/daughters/insert cylinder
/gate/breast_phantom/geometry/setRmin 0. mm
/gate/breast_phantom/geometry/setRmax 35. mm
/gate/breast_phantom/geometry/setHeight 150. mm
/gate/breast_phantom/placement/setRotationAxis 1 0 0
/gate/breast_phantom/placement/setRotationAngle 90. deg
/gate/breast_phantom/setMaterial Breast
```

```
   /gate/breast_phantom/vis/setColor white
   /gate/breast_phantom/vis/forceWireframe
(definition of the phantom)

   Breast: d=1.020 g/cm3 ; n = 8
      +el: name=Oxygen;     f=0.5270
      +el: name=Carbon;     f=0.3320
      +el: name=Hydrogen ;  f=0.1060
      +el: name=Nitrogen;   f=0.0300
      +el: name=Sulfur ;    f=0.0020
      +el: name=Sodium ;    f=0.0010
      +el: name=Phosphor;   f=0.0010
      +el: name=Chlorine ;  f=0.0010
(definition of Breast tissue in the GateMaterials file)
```

All the simulated lesions were spheres defined and placed inside this phantom using similar commands:

```
   /gate/breast_phantom/daughters/name tumor1
   /gate/breast_phantom/daughters/insert sphere
   /gate/tumor1/placement/setTranslation 0. 0. 0. mm
   /gate/tumor1/geometry/setRmin 0. mm
   /gate/tumor1/geometry/setRmax 5. mm
   /gate/tumor1/setMaterial Aluminium
   /gate/tumor1/vis/setColor yellow
(definition of a tumour mass)
```

where "/gate/tumor1/geometry/setRmax" defined the radius of the lesion and "/gate/tumor1/placement/setTranslation" where it was placed.

To test this model all the lesions were defined as being made of aluminium material *(/gate/tumor1/setMaterial Aluminium*).

To retrieve information about the Rayleigh and Compton interactions within the phantom, a sensitive detector (*phantomSD*) is associated with the volume using the following command line:

/gate/breast_phantom/attachPhantomSD

4.2.2 Detector Geometry Definition

4.2.2.1 DBCT Detector Defintion

The design of the DBCT detector was based on the pixelated PaxScan A® 2520D/CL Amorphous Silicon Digital X-Ray Imager [132] with total dimensions of 19.2x24.2x0.4 cm and 0.508x0.508 mm pixels, adapting the code provided by the GATE examples for a correct placement and dimensions to the required simulations:

```
   /gate/world/daughters/name CTscanner
   /gate/world/daughters/insert box
   /gate/CTscanner/placement/setTranslation 0. 0. 100. mm
   /gate/CTscanner/geometry/setXLength 19.3 cm
   /gate/CTscanner/geometry/setYLength 24.2 cm
   /gate/CTscanner/geometry/setZLength 4 mm
   /gate/CTscanner/setMaterial Air
   /gate/CTscanner/vis/forceWireframe
   /gate/CTscanner/vis/setColor white
```

```
  #/gate/CTscanner/moves/insert orbiting
  #/gate/CTscanner/orbiting/setSpeed 1 deg/s
  #/gate/CTscanner/orbiting/setPoint1 0 0 0 cm
  #/gate/CTscanner/orbiting/setPoint2 0 1 0 cm

  #############           ############
  # CTSCANNER #   ---->    #  MODULE  #
  #############           ############
  /gate/CTscanner/daughters/name module
  /gate/CTscanner/daughters/insert box
  /gate/module/geometry/setXLength 19.3 cm
  /gate/module/geometry/setYLength 24.2 cm
  /gate/module/geometry/setZLength  4. mm
  /gate/module/setMaterial Silicon
  /gate/module/vis/forceWireframe
  /gate/module/vis/setColor white

  #############           #############
  #  MODULE  #   ---->    # CLUSTER_0 #
  #############           #############
  /gate/module/daughters/name cluster
  /gate/module/daughters/insert box
  /gate/cluster/geometry/setXLength 19.3 cm
  /gate/cluster/geometry/setYLength 24.2 cm
  /gate/cluster/geometry/setZLength  4. mm
  /gate/cluster/setMaterial Air
  /gate/cluster/vis/forceWireframe
  /gate/cluster/vis/setColor white
  /gate/cluster/vis/setDaughtersInvisible
```

(total scanner definition)

```
  #############             #############           ############
  #  MODULE  #   ---->      # CLUSTER_0 #   ---->    # PIXEL_0 #
  #############             #############           ############
  /gate/cluster/daughters/name pixel
  /gate/cluster/daughters/insert box
  /gate/pixel/geometry/setXLength 0.508 mm
  /gate/pixel/geometry/setYLength 0.508 mm
  /gate/pixel/geometry/setZLength 4 mm
  /gate/pixel/setMaterial Silicon
  #/gate/pixel/vis/setColor red
  #/gate/pixel/vis/forceWireframe
```

(pixel definition)

```
  # REPEAT PIXEl_0
  /gate/pixel/repeaters/insert cubicArray
  /gate/pixel/cubicArray/setRepeatNumberX 379
  /gate/pixel/cubicArray/setRepeatNumberY 475
  /gate/pixel/cubicArray/setRepeatNumberZ 1
  /gate/pixel/cubicArray/setRepeatVector 0.508 0.508 0. mm
  /gate/pixel/cubicArray/autoCenter true
```

(pixel repition along the detector)

```
  # ATTACH SYSTEM
  /gate/systems/CTscanner/module/attach module
  /gate/systems/CTscanner/cluster_0/attach cluster
```

```
/gate/systems/CTscanner/pixel_0/attach pixel

# ATTACH LAYER
/gate/pixel/attachCrystalSD
```

4.2.2.2 SPECT Detector Definition

The SPECT scanner which was used was designed by Dr. Ricardo Capote at IBEB. With 6.40x15.12x18.85 cm as dimensions it was composed by dual-head SPECT cameras with pixelated LYSO crystals of 20x2x2 mm and convergent collimators. The following code illustrates the different levels of definition. First the SPECT system as a whole:

```
##### SPECT  HEAD with shield #####
/gate/world/daughters/name SPECThead
/gate/world/daughters/insert box
/gate/SPECThead/geometry/setXLength 6.40 cm
/gate/SPECThead/geometry/setYLength 15.12 cm
/gate/SPECThead/geometry/setZLength 18.85 cm
/gate/SPECThead/placement/setTranslation -8.2 0. 0. cm
/gate/SPECThead/setMaterial Tungsten
/gate/SPECThead/repeaters/insert ring
/gate/SPECThead/ring/setRepeatNumber 2
/gate/SPECThead/vis/setColor yellow
/gate/SPECThead/vis/forceWireframe
/gate/SPECThead/attachPhantomSD
```

(SPECT scanner definition)

Afterwards its crystals:

```
#### Air Detector BOX ######
/gate/SPECThead/daughters/name airbox
/gate/SPECThead/daughters/insert box
/gate/airbox/geometry/setXLength 2.0 cm
/gate/airbox/geometry/setYLength 14.72 cm
/gate/airbox/geometry/setZLength 18.05 cm
/gate/airbox/placement/setTranslation -2. 0. 0. cm
/gate/airbox/setMaterial Air
/gate/airbox/vis/setColor cyan
/gate/airbox/vis/forceWireframe

##### Detector or Crystal Matrix Volume #####
/gate/airbox/daughters/name crystal
/gate/airbox/daughters/insert box
/gate/crystal/geometry/setXLength 2.0 cm
/gate/crystal/geometry/setYLength 14.72 cm
/gate/crystal/geometry/setZLength 17.02 cm
/gate/crystal/placement/setTranslation 0. 0. 0. cm
/gate/crystal/setMaterial BaSO4
/gate/crystal/vis/setColor green
/gate/crystal/vis/forceWireframe

##### Individual Crystal #####
/gate/crystal/daughters/name pixel
/gate/crystal/daughters/insert box
/gate/pixel/geometry/setXLength 20. mm
```

```
  /gate/pixel/geometry/setYLength 2. mm
  /gate/pixel/geometry/setZLength 2. mm
  /gate/pixel/placement/setTranslation 0. 0. 0. mm
  /gate/pixel/setMaterial LYSO
  /gate/pixel/vis/setColor white
  #/gate/pixel/vis/forceWireframe
```
(definition of a single crystal)

```
  ## Repeat the crystal in an array 74x64
  /gate/pixel/repeaters/insert cubicArray
  /gate/pixel/cubicArray/setRepeatNumberX 1
  /gate/pixel/cubicArray/setRepeatNumberY 64
  /gate/pixel/cubicArray/setRepeatNumberZ 74
  /gate/pixel/cubicArray/setRepeatVector 0. 2.3 2.3 mm
```
(crystal repition along the detector)

Finally, the collimator is defined as:

```
  ##### COLLIMATOR BOX ######
  /gate/SPECThead/daughters/name collimator
  /gate/SPECThead/daughters/insert box
  /gate/collimator/geometry/setXLength 4.20 cm
  /gate/collimator/geometry/setYLength 15.12 cm
  /gate/collimator/geometry/setZLength 18.85 cm
  /gate/collimator/placement/setTranslation 1.1 0. 0. cm
  /gate/collimator/setMaterial Tungsten
  /gate/collimator/vis/setColor black
  /gate/collimator/vis/forceWireframe
  /gate/collimator/attachPhantomSD
```
(collimator definition)

```
  ##### HOLE LINE 1 COLUMN 1 ######
  /gate/collimator/daughters/name hole1c1
  /gate/collimator/daughters/insert trpd
  /gate/hole1c1/geometry/setX1Length 1.89 mm
  /gate/hole1c1/geometry/setY1Length 1.89 mm
  /gate/hole1c1/geometry/setX2Length 1.61 mm
  /gate/hole1c1/geometry/setY2Length 1.61 mm
  /gate/hole1c1/geometry/setZLength 45.00 mm
  /gate/hole1c1/geometry/setXBoxLength 0.01 mm
  /gate/hole1c1/geometry/setYBoxLength 0.01 mm
  /gate/hole1c1/geometry/setZBoxLength 0.01 mm
  /gate/hole1c1/placement/setTranslation 0. -66.96 88.60 mm
  /gate/hole1c1/placement/setRotationAxis -0.1535 0.9804 0.1232
  /gate/hole1c1/placement/setRotationAngle 78.620 deg
  /gate/hole1c1/setMaterial Air
  /gate/hole1c1/vis/setColor cyan
  /gate/hole1c1/vis/forceWireframe
  /gate/hole1c1/attachPhantomSD
```
(single hole collimator definition)

The definition of the holes had to be defined one by one, therefore to simplify this method procedure only one is presented here.

4.2.3 Setting up Physics Processes

The final step before the initialisation of the simulation was the configuration of which physics processes were to be modeled. It was performed with the following code:

```
   /gate/physics/addProcess PhotoElectric
   /gate/physics/processes/PhotoElectric/setModel StandardModel

   /gate/physics/addProcess Compton
   /gate/physics/processes/Compton/setModel PenelopeModel

   /gate/physics/addProcess RayleighScattering
   /gate/physics/processes/RayleighScattering/setModel PenelopeModel

   /gate/physics/addProcess ElectronIonisation
   /gate/physics/processes/ElectronIonisation/setModel  StandardModel
e-

   /gate/physics/addProcess Bremsstrahlung
   /gate/physics/processes/Bremsstrahlung/setModel StandardModel e-

   /gate/physics/addProcess MultipleScattering e-

   /gate/physics/processList Enabled
   /gate/physics/processList Initialized
(physics process to be included in the simulation)
```

4.2.4 Sources Definition

The definition of the source varied from CT to SPECT. For CT the X-ray source has to be defined in GATE as gamma particles. To achieve a realistic condition, a polyenergetic beam was simulated using SpeKCalc version 1.0 with energies ranging from 35 to 80 keV [133, 134]. The output was inserted in the macro file below:

```
   /gate/source/addSource xraygun
   /gate/source/verbose 0
   /gate/source/xraygun/setActivity 5000000. becquerel
   /gate/source/xraygun/gps/verbose 0
   /gate/source/xraygun/gps/particle gamma
   /gate/source/xraygun/gps/energytype Arb
   /gate/source/xraygun/gps/histname arb
   /gate/source/xraygun/gps/emin 35.00 keV
   /gate/source/xraygun/gps/emax 80.00 keV
   /gate/source/xraygun/gps/histpoint  0.035  1187
   /gate/source/xraygun/gps/histpoint  0.036  1281
   /gate/source/xraygun/gps/histpoint  0.037  1364
   /gate/source/xraygun/gps/histpoint  0.038  1438
   /gate/source/xraygun/gps/histpoint  0.039  1500
   /gate/source/xraygun/gps/histpoint  0.040  1553
   /gate/source/xraygun/gps/histpoint  0.041  1595
   /gate/source/xraygun/gps/histpoint  0.042  1629
   /gate/source/xraygun/gps/histpoint  0.043  1653
   /gate/source/xraygun/gps/histpoint  0.044  1669
   /gate/source/xraygun/gps/histpoint  0.045  1675
```

```
/gate/source/xraygun/gps/histpoint  0.046  1676
/gate/source/xraygun/gps/histpoint  0.047  1670
/gate/source/xraygun/gps/histpoint  0.048  1658
/gate/source/xraygun/gps/histpoint  0.049  1641
/gate/source/xraygun/gps/histpoint  0.050  1618
/gate/source/xraygun/gps/histpoint  0.051  1592
/gate/source/xraygun/gps/histpoint  0.052  1558
/gate/source/xraygun/gps/histpoint  0.053  1525
/gate/source/xraygun/gps/histpoint  0.054  1488
/gate/source/xraygun/gps/histpoint  0.055  1451
/gate/source/xraygun/gps/histpoint  0.056  1407
/gate/source/xraygun/gps/histpoint  0.057  1364
/gate/source/xraygun/gps/histpoint  0.058  1805
/gate/source/xraygun/gps/histpoint  0.059  2125
/gate/source/xraygun/gps/histpoint  0.060  1226
/gate/source/xraygun/gps/histpoint  0.061  1178
/gate/source/xraygun/gps/histpoint  0.062  1127
/gate/source/xraygun/gps/histpoint  0.063  1077
/gate/source/xraygun/gps/histpoint  0.064  1026
/gate/source/xraygun/gps/histpoint  0.065  974
/gate/source/xraygun/gps/histpoint  0.066  922
/gate/source/xraygun/gps/histpoint  0.067  1175
/gate/source/xraygun/gps/histpoint  0.068  816
/gate/source/xraygun/gps/histpoint  0.069  845
/gate/source/xraygun/gps/histpoint  0.070  688
/gate/source/xraygun/gps/histpoint  0.071  635
/gate/source/xraygun/gps/histpoint  0.072  583
/gate/source/xraygun/gps/histpoint  0.073  529
/gate/source/xraygun/gps/histpoint  0.074  475
/gate/source/xraygun/gps/histpoint  0.075  418
/gate/source/xraygun/gps/histpoint  0.076  356
/gate/source/xraygun/gps/histpoint  0.077  294
/gate/source/xraygun/gps/histpoint  0.078  231
/gate/source/xraygun/gps/histpoint  0.079  128
/gate/source/xraygun/gps/histpoint  0.080  0
/gate/source/xraygun/gps/arbint Lin
/gate/source/xraygun/gps/type Plane
/gate/source/xraygun/gps/shape Rectangle
/gate/source/xraygun/gps/halfx 0.5 mm
/gate/source/xraygun/gps/halfy 0.5 mm
/gate/source/xraygun/gps/mintheta 0  deg
/gate/source/xraygun/gps/maxtheta  20 deg
/gate/source/xraygun/gps/centre 0. 0 -30. cm
/gate/source/xraygun/gps/angtype iso
/gate/source/list
```

(CT source definition)

On the other hand, for SPECT there was no need to use external programs and the sources emitting gamma radiation of 140 keV for the phantom background and the lesions were defined as followed:

```
/gate/source/addSource cylinder
/gate/source/cylinder/gps/type Volume
/gate/source/cylinder/gps/shape Cylinder
/gate/source/cylinder/gps/radius 35. mm
```

```
/gate/source/cylinder/gps/halfz 75. mm
/gate/source/cylinder/gps/centre 0. 0. 0. mm
/gate/source/cylinder/gps/particle gamma
/gate/source/cylinder/gps/energy 140. keV
/gate/source/cylinder/setActivity 577267650. Bq
/gate/source/cylinder/gps/angtype iso
/gate/source/cylinder/attachTo breast_phantom
/gate/source/list
```

(source definition for the phantom)

```
/gate/source/addSource lesion1
/gate/source/lesion1/gps/type Volume
/gate/source/lesion1/gps/shape Sphere
/gate/source/lesion1/gps/radius 5. mm
/gate/source/lesion1/gps/centre 0. 0. 0. mm
/gate/source/lesion1/gps/particle gamma
/gate/source/lesion1/gps/energy 140. keV
/gate/source/lesion1/setActivity 5235990. Bq
/gate/source/lesion1/gps/angtype iso
/gate/source/lesion1/attachTo breast_phantom
/gate/source/list
```

(source definition for tumour masses)

4.2.5 Digitizer Parameters Definition

The digitizer allows to introduce energy cuts and other variation reduction techniques. For SPECT X-ray below 10 keV were not considered and for SPECT the photons which were considered were between 126 keV and 165 keV.

```
#############
# DIGITIZER #
#############
/gate/digitizer/Singles/insert adder
/gate/digitizer/Singles/insert readout
/gate/digitizer/Singles/readout/setDepth 2
/gate/digitizer/Singles/insert thresholder
/gate/digitizer/Singles/thresholder/setThreshold 10. keV
```

(CT digitizer)

```
#############
# DIGITIZER #
#############
/gate/digitizer/Singles/insert adder
/gate/digitizer/Singles/insert readout
/gate/digitizer/Singles/readout/setDepth 2

#### ENERGY BLURRING ####

/gate/digitizer/Singles/insert blurring
/gate/digitizer/Singles/blurring/setResolution 0.15
/gate/digitizer/Singles/blurring/setEnergyOfReference 140. keV

####  ENERGY CUT  ####
```

```
/gate/digitizer/Singles/insert thresholder
/gate/digitizer/Singles/thresholder/setThreshold 126. keV
/gate/digitizer/Singles/insert upholder
/gate/digitizer/Singles/upholder/setUphold 165. keV
```

(SPECT digitizer)

4.2.6 Output Format Definition

To allow for a certain homogeneity in result analysis, .root files were defined as the output format for both modalities using the following macro file:

```
########
# ROOT #
########
/gate/output/root/enable
/gate/output/root/setFileName outputFile
/gate/output/root/setRootSinglesAdderFlag 1
/gate/output/root/setRootSinglesBlurringFlag 1
/gate/output/root/setRootSinglesThresholderFlag 1
/gate/output/root/setRootSinglesUpholderFlag 1
```

(root ouput file definition)

4.2.7 Acquisition Parameters Definition

The final step of a GATE MC simulation is the definition of the acquisition parameters which differ not only from CT to SPECT, but also to test different acquisition conditions.

In a macro GATE file this step is easily performed by simply using the following commands below:

/gate/application/setTimeSlice 1. s
/gate/application/setTimeStart 0. s
/gate/application/setTimeStop 1. s
S T A R T the A C Q U I S I T I O N
/gate/application/startDAQ

In order to perform this, the beginning and the end of the acquisition are defined with */gate/application/setTimeStart* and /gate/application/setTimeStop, respectively. To determine the number of projections of the simulation:

$$N_{run} = \frac{setTimeStop - setTimeStart}{setTimeSlice} \qquad \text{(Eq. 4.2.7.1)}$$

where the command /gate/application/setTimeSlice refers to the slice duration, which is the same for every slice.

In the next section the procedure followed for CT and SPECT image reconstruction will be addressed, particularly using C++ and MATLAB® for CT and C and MATLAB® for SPECT.

4.3 Image Reconstruction

After the completion of the simulations the image reconstruction process was conducted using two steps for both CT and SPECT. First, the information from the output files using C++ for CT and C for SPECT was extracted and ordered. Afterwards, a MATLAB® script performed the 3D image reconstruction using FBP for CT and MLEM for SPECT.

4.3.1 CT

For CT pre-processing an executable was compiled from a C++ file. The main function of the program was to extract the values for each projection using dedicated root commands and illustrate the projection results using histogram designed within the program to a specific Canvas. The values which were extracted in this step were stored for purpose reconstructions using a MATLAB® reconstruction script.

After this preprocessing step, 3D reconstruction was performed with a MATLAB® script that after loading the extracted projection values, applied the logarithm to all the values of each projection. FBP was the algorithm used for reconstruction by applying the functions *fan2para* and *iradon*. The function *fan2para* converts the fan beam to parallel beam, using this arguments:

```
fan2para(proj, 590.551, 'FanSensorGeometry', 'line', 'ParallelCoverage', 'cycle');
```

where *proj* are the projection values, *590.551* is the distance, in pixels, from the fan beam vertex to the centre of rotation, *'FanSensorGeometry'* and *'line'* allow to define the detector as a plane detector and finally *'ParallelCoverage'* and *'cycle'* accounts for the fact that the projections must cover 360º degrees.

The function *iradon*, as the name suggest is the inverse of the radon transform with the following parameters:

```
iradon(par_Values, theta, 'none', 'none', 'none', 380);
```

where *par_Values* are the values for each projection obtained in the previous step, *theta* is a vector with the projection angles, *'none'* is used for the function to assume the default value, in order to be able to include a final parameter which is the output size, in this case the number of pixels in a certain direction, to be the final dimensions of the reconstructed values.

Finally, after conducting image reconstruction, a GIF was created to visualize the results, which were also stored in a .mat file for posterior quantification metrics evaluation.

4.3.2 SPECT

For SPECT, a pre-processing .C file was used to extract the values for each projection using dedicated root commands, storing those values for purpose reconstructions using a MATLAB® reconstruction script.

After this preprocessing step, 3D reconstruction was acquired with a MATLAB® script that after loading the extracted projection values, applied the logarithm to all the values of each projection. MLEM was the algorithm used for 3D reconstruction of SPECT images.

Both these two files were designed by Dr. Ricardo Capote (ref) and applied unchanged to the simulations which were performed.

4.4 Image Analysis

After reconstructing the images through the correspondent projects, several metrics were applied to evaluate the results obtained. For CT it was applied to the reconstructed image. For SPECT, since the algorithm created by Dr. Ricardo Capote was validated in his PhD thesis and the results were not as expected these metrics were not applied.

$$Contrast = \frac{Mean_{Mass} - Mean_{Phantom}}{Mean_{Mass} + Mean_{Phantom}} \quad \text{(Eq. 4.4.1)}$$

where $Mean_{Mass}$ is the mean value for the area values of a certain mass and $Mean_{Phantom}$ in an area of the phantom that don't have masses.

$$CNR = \frac{Mean_{Mass} - Mean_{Phantom}}{\sigma_{Mass}} \quad \text{(Eq. 4.4.2)}$$

where $Mean_{Mass}$ is the mean value for the area values of a certain mass, $Mean_{Phantom}$ in an area of the phantom that don't have masses and σ_{Mass} is the standard deviation of the area values of a certain mass.

5 Results and Discussions

5.1 - CT

After the conclusion of the simulation and the combination of the .root generated files, some histograms were made using root specific commands in order to visualise if the projections that were acquired were as expected as portrayed in figure 5.1.1.

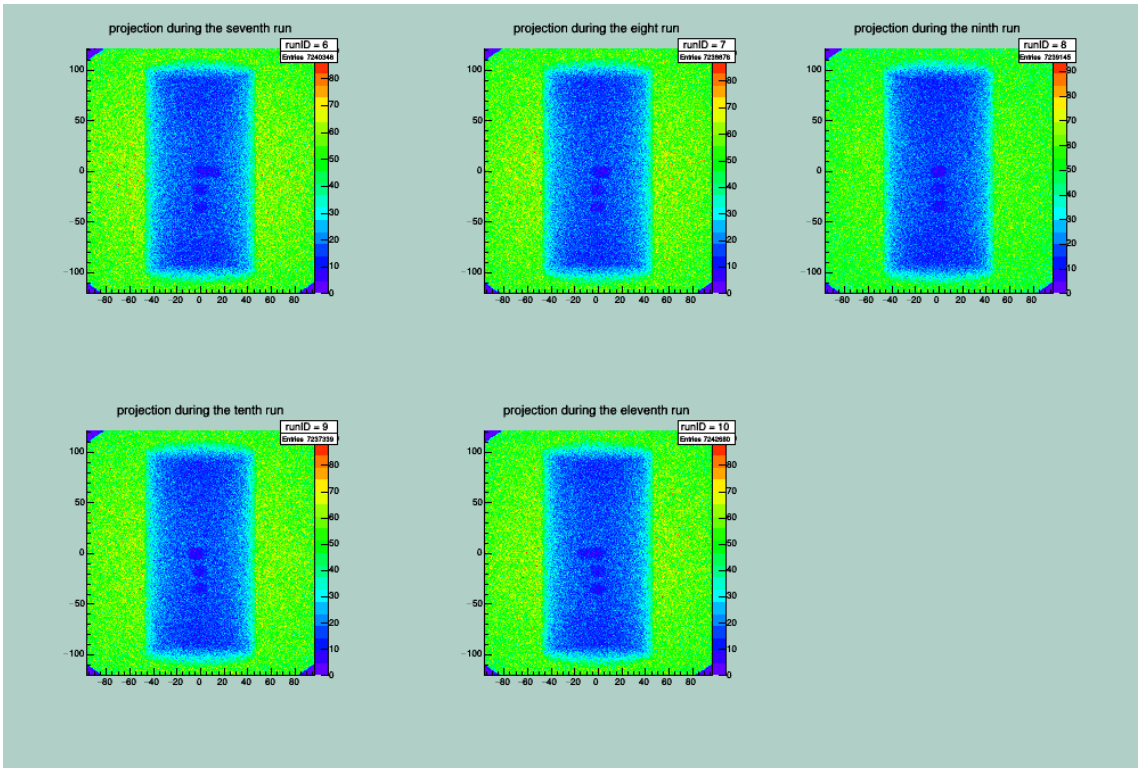

Figure 5.1.1. - Root histograms of the acquired projections. For illustration purposes the projections represented only range from the seventh to the eleventh run.

In this image is explicit that the projections acquired are from different angles, which is easily identifiable due to the relative position of the masses inside the phantom.

The image reconstruction algorithm is applied to the extracted projection values and the result of the reconstruction is visualized using MATLAB® function *imshow*.

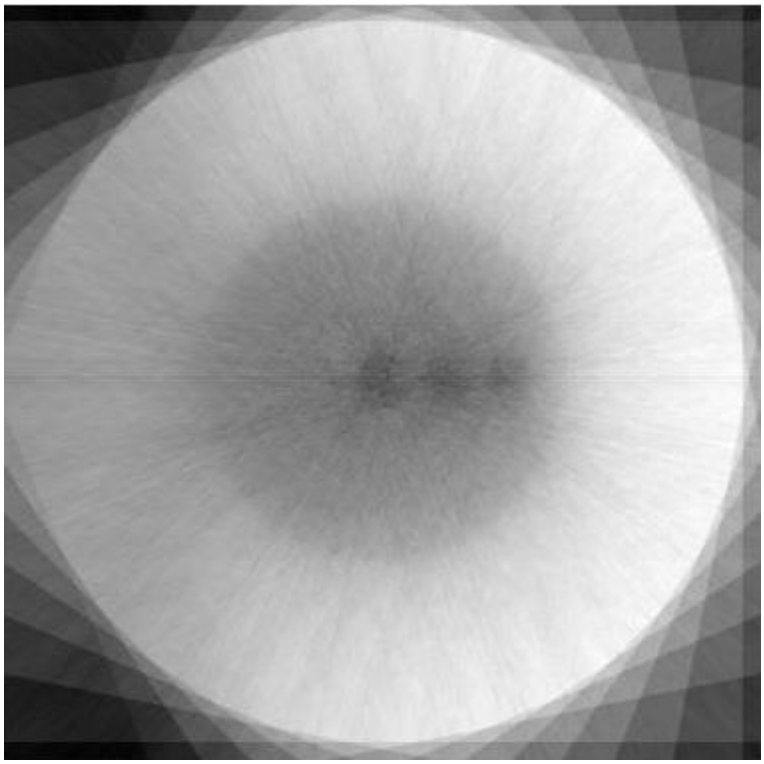

Figure 5.1.2. - Axial slice of the final reconstructed image at the centre of the phantom.

With this image slice can be clearly identified three masses in the same x axis, despite the fact that there is a considerable image degradation with the radial distance from the centre to the periphery.

The following image illustrate a plane where can only be seen one mass, easily identifiable by the different coloration when compared to the phantom and its circular geometry, resultant of the slice cut.

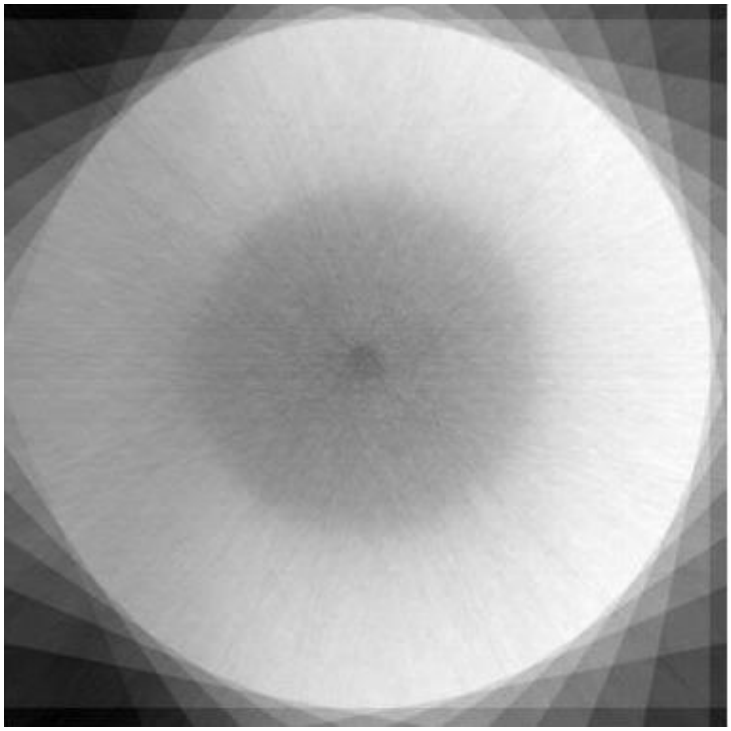

Figure 5.1.3. - Axial slice of the final reconstructed image with a 13 mm distance to the centre of the phantom in the z axis.

Finally, for visualisation purposes, an coronal slice of the centre of the reconstructed image was obtained using the same function (see figure 5.1.4), where the different masses can be clearly identified along the x and z axis and that the phantom almost fully occupies the FOV.

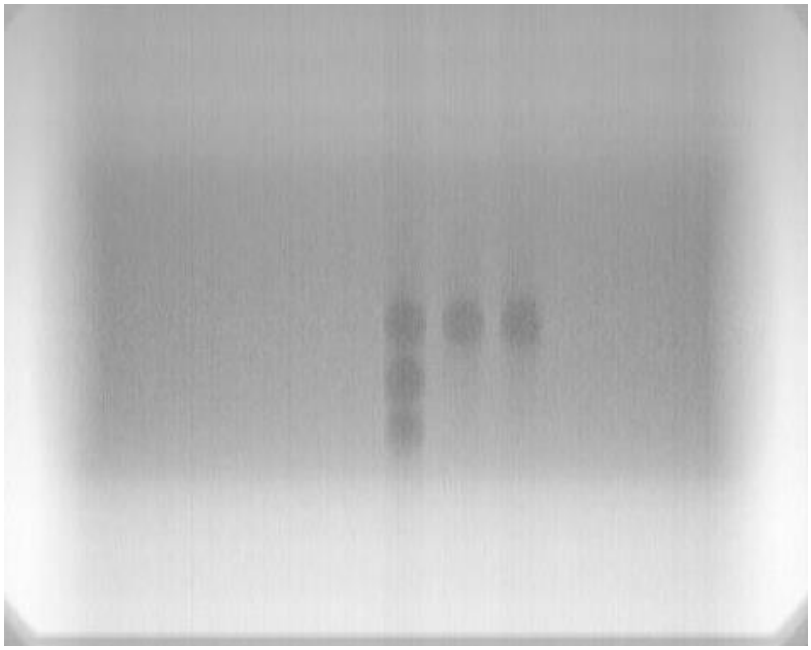

Figure 5.1.4. - Coronal image slice of centre of the final reconstructed image.

Given the fact that the areas of the lesions are known, comparative and non-absolut metrics were calculated to verify and validate the simulation results, despite the fact that the reconstruction method doesn't have any methods that would allow an improved image reconstruction.

Contrast and contrast to noise ratio were calculated and compared along the two different axis with respect to the distance to the centre, where a mass, common to both comparisons, is placed.

Figures 5.1.5 to 5.1.8 graphically represent the contrast and contrast to noise to ratio along the different axis. As expected, the results clearly demonstrate a decay in image quality from the centre to the periphery of the phantom, especially in x axis.

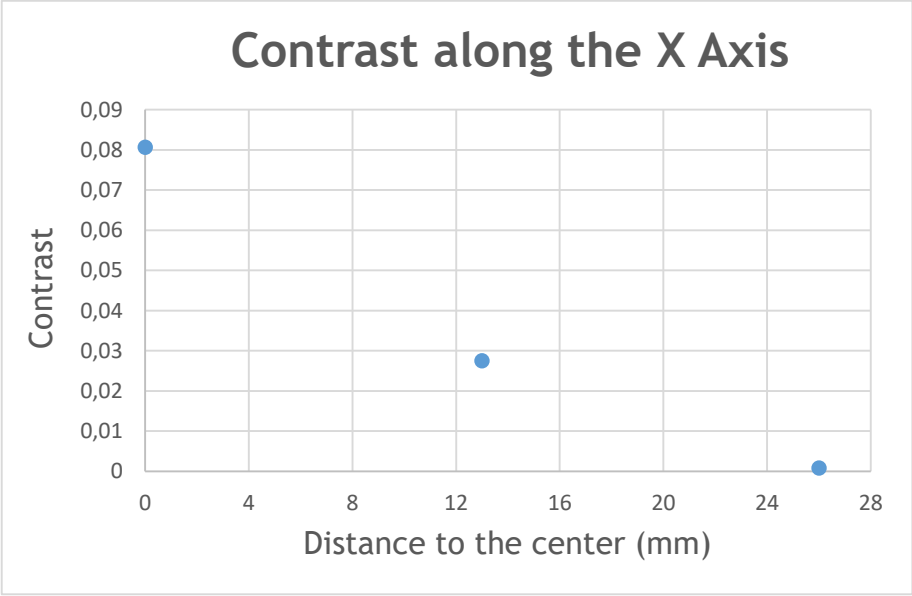

Figure 5.1.5. - Contrast along the x axis.

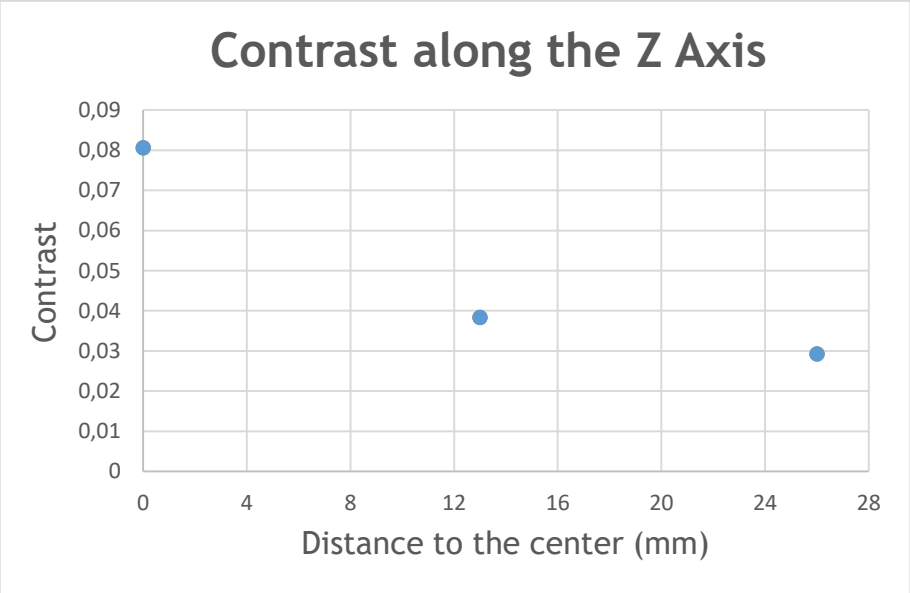

Figure 5.1.6. - Contrast along the z axis.

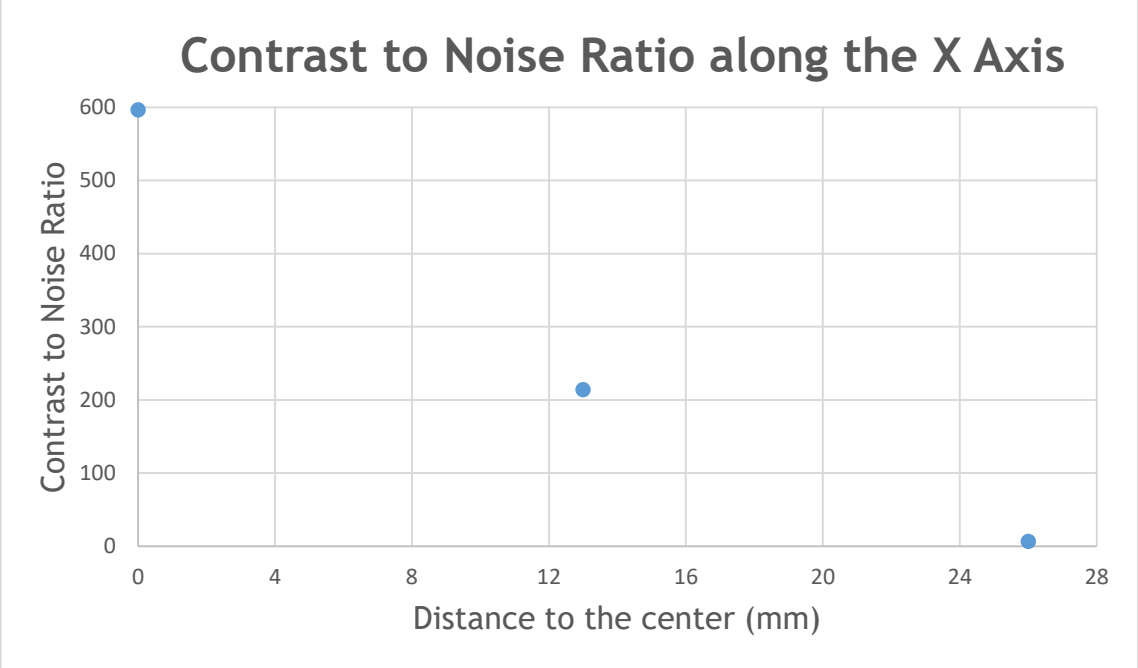

Figure 5.1.7. - Contrast to noise ratio along the x axis.

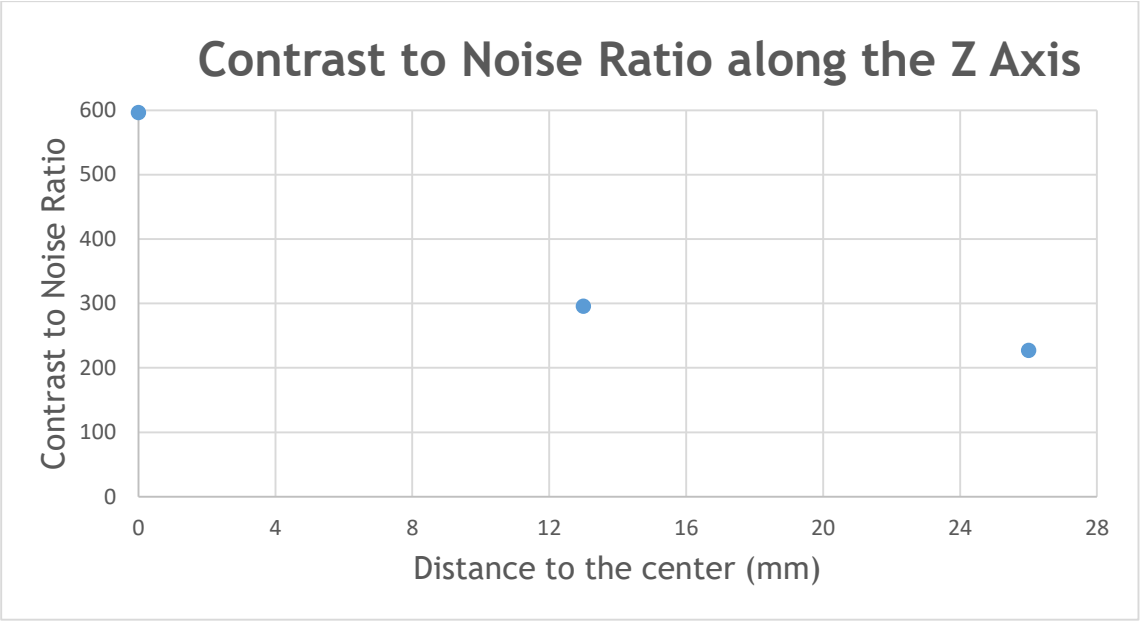

Figure 5.1.8. - Contrast to noise ratio along the z axis.

This image degradation is caused not only by the presence of stochastic physical phenomena, but also by the fact that no corrections were considered in the reconstruction process, improving the final result. In particular, for the x axis, the additional image degradation when compared to the z axis, might be correlated with the different distances of the masses to the detector according to the different projection angles.

5.2 – SPECT

Using the detector and acquisition parameters of the simulations conducted by Dr. Ricardo Capote, changing only the phantom, the .root files were read in order to extract the projection values with the code implemented by Dr. Ricardo Capote with a few minor modifications to a file that was afterwards loaded in a MATLAB® script, which implemented MLEM, modifying only the input files and the results visualisation.

Figure 5.2.1 – SPECT simulation results. The image shows the different projections of the phantom.

As can be seen from the image above, the results obtained were not conclusive, thus the metrics used for CT were not applied to SPECT to evaluate relatively the quality of the images produced.

The following chapter will present the conclusions and final remarks regarding the realisation and implementation of this work.

6 Conclusions and Future Work

In this work, a framework was implemented to conduct MC simulations and reconstruct 3D images with the resultant files for two different imaging systems that could complement the other. Along the development process, and especially for image reconstruction and image analysis there was a major concern regarding the homogenisation of the procedure for both imaging modalities as much as possible.

The results for CT prove its feasibility and validate it as a possible research tool in an area so important as breast cancer diagnosis.

Using the model that was already developed by Dr. Ricardo Capote, the work performed in this dissertation is not restricted to the imaging results, but more importantly, that by following the methodology presented here, the usage of this model could be replicated in other studies of optimization of MC simulations or image reconstruction or even as a starting point for GATE new users.

This could be pursued using voxelised phantoms, that would allow GPU computation, reducing the computation time by taking advantage of the great number of processors in NVIDIA graphics cards, which could use CUDA software to accelerate MC simulations.

To address a possible cross talk between the two systems, MC simulations could also be developed with GATE using this work as a base in order to evaluate if one system interferes with the other system's performance.

Finally, in order to do proper optimization studies, more realistic conditions should be created with the development of MC simulations with more complex phantoms and accurate material and density, especially when referring to tumours.

Bibliography

[1] László Tabár, Bedrich Vitak, Hsiu-Hsi Tony Chen, Stephen W. Du_y, Ming-Fang Yen, Ching-Feng Chiang, Ulla Brith Krusemo, Tibor Tot, and Robert A. Smith. "The Swedish Two-County Trial twenty years later. Updated mortality results and new insights from long-term follow-up." Radiologic Clinics of North America, 38(4):625-651, July 2000.
[2] László Tabár, Ming-Fang Yen, Bedrich Vitak, Hsiu-Hsi Tony Chen, Robert A. Smith, and Stephen W. Du_y. "Mammography service screening and mortality in breast cancer patients: 20-year follow-up before and after introduction of screening." The Lancet, 361(9367):1405-1410, April 2003.
[3] Zhao B, Zhang X, Cai W, Conover D and Ning R. "Cone beam breast CT with multiplanar and three dimensional visualization in differentiating breast masses compared with mammography". Eur. J. Radiol. 84 48–53. 2015.
[4] K. O'Connor, "Molecular breast imaging: An emerging modality for breast cancer screening,". Breast Cancer Manage. 4(1), 33–40. 2015.
[5] Moon WK, Lo CM, Goo JM, et al. "Quantitative analysis for breast density estimation in low dose chest CT scans." J Med Syst 21:38. 2014.
[6] Mettivier G, Russo P, Cesarelli M, et al. "Dedicated scanner for laboratory investigations on cone-beam CT/SPECT imaging of the breast". Nucl Instrum Methods Phys Res A. 629:350–356. 2011.
[7] American Cancer Society. "Detailed Guide: Breast Cancer", 2014.
[8] National Cancer Institute. "What You Need To Know About TM Breast Cancer", April 2012.
[9] Tibor Tot. "The Theory of the Sick Breast Lobe and the Possible Consequences". International Journal of Surgical Pathology, 15(4):369–375, October 2007.
[10] International Agency for Research on Cancer (IARC) and World Health Organization (WHO). "GLOBOCAN 2012: Estimated cancer incidence, mortality and prevalence worldwide in 2012". Retrieved on dec 3 rd , 2014.
[11] American Cancer Society. "Global Cancer Facts & Figures." 3rd Edition. Atlanta: American Cancer Society. 2015.
[12] Direcção-Geral da Saúde. "Portugal Doenças Oncológicas em números – 2014". November 2014.
[13] Instituto Nacional de Estatística. "Estatísticas no Feminino: Ser Mulher em Portugal 2001-2011", 2012.
[14] David Gur, Gordon S. Abrams, Denise M. Chough, Marie A. Ganott, Christiane M. Hakim, Ronald L. Perrin, Grace Y. Rathfon, Jules H. Sumkin, Margarita L. Zuley, and Andriy I. Bandos. "Digital breast tomosynthesis: observer performance study". AJR. American journal of roentgenology, 193(2):586-591, August 2009.
[15] Karen K. Lindfors, John M. Boone, Thomas R. Nelson, Kai Yang, Alexander L. C. Kwan, and DeWitt F. Miller. "Dedicated breast CT: initial clinical experience". Radiology, 246(3):725-733, March 2008.
[16] M. O. Leach, C. R. M. Boggis, A. K. Dixon, D. F. Easton, R. A. Eeles, D. G. R. Evans, F. J. Gilbert, I. Griebsch, R. J. C. Ho, P. Kessar, S. R. Lakhani, S. M. Moss, A. Nerurkar, A. R. Padhani, L. J. Pointon, D. Thompson, R. M. L. Warren, and MARIBS study group. "Screening with magnetic resonance imaging and mammography of a UK population at high familial risk of breast cancer: a prospective multicentre cohort study (MARIBS)". Lancet, 365(9473):1769-1778, May 2005.
[17] B. Bagni, A. Franceschetto, A. Casolo, M. De Santis, I. Bagni, F. Pansini, and C. Di Leo. "Scintimammography with 99mTc-MIBI and magnetic resonance imaging in the evaluation of breast cancer". European Journal of Nuclear Medicine and Molecular Imaging, 30(10):1383-1388, October 2003.

[18] Christiane K. Kuhl, Simone Schrading, Claudia C. Leutner, Nuschin Morakkabati-Spitz, Eva Wardelmann, Rolf Fimmers, Walther Kuhn, and Hans H. Schild. “Mammography, breast ultrasound, and magnetic resonance imaging for surveillance of women at high familial risk for breast cancer”. Journal of Clinical Oncology: Official Journal of the American Society of Clinical Oncology, 23(33):8469-8476, November 2005.
[19] Wendie A. Berg, Je_rey D. Blume, Jean B. Cormack, Ellen B. Mendelson, Daniel Lehrer, Marcela Böhm-V_elez, Etta D. Pisano, Roberta A. Jong, W. Phil Evans, Marilyn J. Morton, Mary C. Mahoney, Linda Hovanessian Larsen, Richard G. Barr, Dione M. Farria, Helga S. Marques, Karan Boparai, and ACRIN 6666 Investigators. “Combined screening with ultrasound and mammography vs mammography alone in women at elevated risk of breast cancer”. JAMA, 299(18):2151-2163, May 2008.
[20] Carrie B. Hruska, Judy C. Boughey, Stephen W. Phillips, Deborah J. Rhodes, Dietlind L. Wahner-Roedler, Dana H. Whaley, Amy C. Degnim, and Michael K. O'Connor. “Scientific Impact Recognition Award: Molecular breast imaging: a review of the mayo Clinic Experience”. American Journal of Surgery, 196(4):470-476, October 2008.
[21] Wendie A. Berg, Irving N.Weinberg, Deepa Narayanan, Mary E. Lobrano, Eric Ross, Laura Amodei, Lorraine Tafra, Lee P. Adler, Joseph Uddo, William Stein, Edward A. Levine, and Positron Emission Mammography Working Group. “High-resolution fluorodeoxyglucose positron emission tomography with compression (“positron emission mammography”) is highly accurate in depicting primary breast cancer”. The Breast Journal, 12(4):309-323, August 2006.
[22] Edward A. Levine, Rita I. Freimanis, Nancy D. Perrier, Kathryn Morton, Nadia M. Lesko, Simon Bergman, Kim R. Geisinger, Rodney C. Williams, Connie Sharpe, Valera Zavarzin, Irving N. Weinberg, Pavel Y. Stepanov, David Beylin, Kathryn Lauckner, Mohan Doss, Judy Lovelace, and Lee P. Adler. “Positron emission mammography: initial clinical results”. Annals of Surgical Oncology, 10(1):86-91, February 2003.
[23] Joann G. Elmore. “Screening for Breast Cancer”. JAMA, 293(10):1245, March 2005.
[24] D. S. M. Buist, P. L. Porter, C. Lehman, S. H. Taplin, and E. White. “Factors Contributing to Mammography Failure in Women Aged 40-49 Years”. JNCI Journal of the National Cancer Institute, 96(19):1432-1440, October 2004.
[25] American Cancer Society. “Understanding your mammogram report - BI-RADS categories”, 8th December 2014, last revised 9th April 2015. Accessed at http://www.cancer.org/treatment/understandingyourdiagnosis/examsandtestdescriptions/mammogramsandotherbreastimagingprocedures/mammograms-and-other-breast-imaging-procedures-mammo-report on 23rd July 2015.
[26] Linda L. Humphrey, Mark Helfand, Benjamin K. S. Chan, and Steven H. Woolf. “Breast cancer screening: a summary of the evidence for the U.S. Preventive Services Task Force”. Annals of Internal Medicine, 137(5 Part 1):347-360, September 2002.
[27] M. T. Mandelson, N. Oestreicher, P. L. Porter, D. White, C. A. Finder, S. H. Taplin, and E. White. “Breast density as a predictor of mammographic detection: comparison of interval- and screen-detected cancers". Journal of the National Cancer Institute, 92(13):1081-1087, July 2000.
[28] Patricia A. Carney, Diana L. Miglioretti, Bonnie C. Yankaskas, Karla Kerlikowske, Robert Rosenberg, Carolyn M. Rutter, Berta M. Geller, Linn A. Abraham, Steven H. Taplin, Mark Dignan, Gary Cutter, and Rachel Ballard-Barbash. “Individual and combined effects of age, breast density, and hormone replacement therapy use on the accuracy of screening mammography”. Annals of Internal Medicine, 138(3):168-175, February 2003.
[29] David Gur, Gordon S. Abrams, Denise M. Chough, Marie A. Ganott, Christiane M. Hakim, Ronald L. Perrin, Grace Y. Rathfon, Jules H. Sumkin, Margarita L. Zuley, and Andriy I. Bandos. “Digital breast

tomosynthesis: observer performance study". AJR. American journal of roentgenology, 193(2):586-591, August 2009.
[30] James T. Dobbins and Devon J. Godfrey. "Digital x-ray tomosynthesis: current state of the art and clinical potential". Physics in Medicine and Biology, 48(19):R65-106, October 2003.
[31] Steven P. Poplack, Tor D. Tosteson, Christine A. Kogel, and Helene M. Nagy. "Digital breast tomosynthesis: initial experience in 98 women with abnormal digital screening mammography". AJR. American journal of roentgenology, 189(3):616-623, September 2007.
[32] L. T. Niklason, B. T. Christian, L. E. Niklason, D. B. Kopans, D. E. Castleberry, B. H. Opsahl-Ong, C. E.Landberg, P. J. Slanetz, A. A. Giardino, R. Moore, D. Albagli, M. C. DeJule, P. F. Fitzgerald, D. F. Fobare, B. W. Giambattista, R. F. Kwasnick, J. Liu, S. J. Lubowski, G. E. Possin, J. F. Richotte, C. Y. Wei, and R. F. Wirth. "Digital tomosynthesis in breast imaging". Radiology, 205(2):399-406, November 1997.
[33] T. M. Svahn, D. P. Chakraborty, D. Ikeda, S. Zackrisson, Y. Do, S. Mattsson, and I. Andersson. "Breast tomosynthesis and digital mammography: a comparison of diagnostic accuracy". The British Journal of Radiology, 85(1019): 1074-1082, November 2012.
[34] Avice M. O'Connell, Andrew Karellas, and Srinivasan Vedantham. "The Potential Role of Dedicated 3D Breast CT as a Diagnostic Tool: Review and Early Clinical Examples". The Breast Journal, 20(6):592-605, November 2014.
[35] E. Tohno, D. O. Cosgrove, and J. P. Sloane. "Ultrasound Diagnosis of Breast Diseases". Churchill Livingstone, 1994.
[36] Hui Zhi, Bing Ou, Bao-Ming Luo, Xia Feng, Yan-Ling Wen, and Hai-Yun Yang. "Comparison of ultrasound elastography, mammography, and sonography in the diagnosis of solid breast lesions". Journal of Ultrasound in Medicine: Official Journal of the American Institute of Ultrasound in Medicine, 26(6):807-815, June 2007.
[37] G. Rizzatto, R. Chersevani, M. Abbona, V. L. Lombardo, and D. Macorig. "High-resolution sonography of breast carcinoma". European Journal of Radiology, 24(1):11-19, January 1997.
[38] L. Bartella, C. S. Smith, D. D. Dershaw, and L. Liberman. "Imaging breast cancer". Radiologic Clinics of North America, 45(1):45-67, January 2007.
[39] Andrew Karellas and Srinivasan Vedantham. "Breast cancer imaging: a perspective for the next decade". Medical Physics, 35(11):4878-4897, November 2008.
[40] Wendie A. Berg, Jeffrey D. Blume, Jean B. Cormack, Ellen B. Mendelson, Daniel Lehrer, Marcela Böhm-Velez, Etta D. Pisano, Roberta A. Jong, W. Phil Evans, Marilyn J. Morton, Mary C. Mahoney, Linda Hovanessian Larsen, Richard G. Barr, Dione M. Farria, Helga S. Marques, Karan Boparai, and ACRIN 6666 Investigators. "Combined screening with ultrasound and mammography vs mammography alone in women at elevated risk of breast cancer". JAMA, 299(18):2151-2163, May 2008.
[41] Constance D. Lehman, Claudine Isaacs, Mitchell D. Schnall, Etta D. Pisano, Susan M. Ascher, Paul T. Weatherall, David A. Bluemke, Deborah J. Bowen, P. Kelly Marcom, Deborah K. Armstrong, Susan M. Domchek, Gail Tomlinson, Steven J. Skates, and Constantine Gatsonis. "Cancer yield of mammography, MR, and US in high-risk women: prospective multi-institution breast cancer screening study". Radiology, 244(2):381-388, August 2007.
[42] Christopher C. Riedl, Lothar Ponhold, Daniel Flory, Michael Weber, Regina Kroiss, Teresa Wagner, Michael Fuchsjager, and Thomas H. Helbich. "Magnetic resonance imaging of the breast improves detection of invasive cancer, preinvasive cancer, and premalignant lesions during surveillance of women at high risk for breast cancer". Clinical Cancer Research: An Official Journal of the American Association for Cancer Research, 13(20):6144-6152, October 2007.
[43] Debbie Saslow, Carla Boetes, Wylie Burke, Steven Harms, Martin O. Leach, Constance D. Lehman, Elizabeth Morris, Etta Pisano, Mitchell Schnall, Stephen Sener, Robert A. Smith, Ellen

Warner, Martin Yae, Kimberly S. Andrews, Christy A. Russell, and American Cancer Society Breast Cancer Advisory Group. "American Cancer Society guidelines for breast screening with MRI as an adjunct to mammography". CA: a cancer journal for clinicians, 57(2):75-89, April 2007.
[44] Mieke Kriege, Cecile T. M. Brekelmans, Carla Boetes, Peter E. Besnard, Harmine M. Zonderland, Inge Marie Obdeijn, Radu A. Manoliu, Theo Kok, Hans Peterse, Madeleine M. A. Tilanus-Linthorst, Sara H. Muller, Sybren Meijer, Jan C. Oosterwijk, Louk V. A. M. Beex, Rob A. E. M. Tollenaar, de Harry J. Koning, Emiel J. T. Rutgers, Jan G. M. Klijn, and Magnetic Resonance Imaging Screening Study Group. "E_cacy of MRI and mammography for breast-cancer screening in women with a familial or genetic predisposition". The New England Journal of Medicine, 351(5):427-437, July 2004.
[45] M. O. Leach, C. R. M. Boggis, A. K. Dixon, D. F. Easton, R. A. Eeles, D. G. R. Evans, F. J. Gilbert, I. Griebsch, R. J. C. Ho_, P. Kessar, S. R. Lakhani, S. M. Moss, A. Nerurkar, A. R. Padhani, L. J. Pointon, D. Thompson, R. M. L. Warren, and MARIBS study group. "Screening with magnetic resonance imaging and mammography of a UK population at high familial risk of breast cancer: a prospective multicentre cohort study (MARIBS)". Lancet, 365(9473):1769-1778, May 2005.
[46] B. Bagni, A. Franceschetto, A. Casolo, M. De Santis, I. Bagni, F. Pansini, and C. Di Leo. "Scintimammography with ^{99m}Tc-MIBI and magnetic resonance imaging in the evaluation of breast cancer". European Journal of Nuclear Medicine and Molecular Imaging, 30(10):1383-1388, October 2003.
[46] Greg O. Cron, Frederick Kelcz, and Giles E. Santyr. "Improvement in breast lesion characterization with dynamic contrast-enhanced MRI using pharmacokinetic modeling and bookend T(1) measurements". Magnetic Resonance in Medicine: Official Journal of the Society of Magnetic Resonance in Medicine / Society of Magnetic Resonance in Medicine, 51(5):1066-1070, May 2004.
[47] Edna Furman-Haran, Edna Schechtman, Frederick Kelcz, Kevin Kirshenbaum, and Hadassa Degani. "Magnetic resonance imaging reveals functional diversity of the vasculature in benign and malignant breast lesions". Cancer, 104(4):708-718, August 2005.
[48] P. J. Kneeshaw, M. Lowry, D. Manton, A. Hubbard, P. J. Drew, and L. W. Turnbull. "Differentiation of benign from malignant breast disease associated with screening detected microcalcifications using dynamic contrast enhanced magnetic resonance imaging". Breast (Edinburgh, Scotland), 15(1):29-38, February 2006.
[49] Ellen Warner, Hans Messersmith, Petrina Causer, Andrea Eisen, Rene Shumak, and Donald Plewes. "Systematic review: using magnetic resonance imaging to screen women at high risk for breast cancer". Annals of Internal Medicine, 148(9):671-679, May 2008.
[50] Noam Nissan, Edna Furman-Haran, Myra Shapiro-Feinberg, Dov Grobgeld, and Hadassa Degani. "Diffusion-tensor MR imaging of the breast: hormonal regulation". Radiology, 271(3):672-680, June 2014.
[51] Savannah C. Partridge, Revathi S. Murthy, Ali Ziadloo, Steven W. White, Kimberly H. Allison, and Constance D. Lehman. "Di_usion tensor magnetic resonance imaging of the normal breast". Magnetic Resonance Imaging, 28(3):320-328, April 2010.
[52] A. Taglia_co, G. Rescinito, F. Monetti, A. Villa, F. Chiesa, E. Fisci, D. Pace, and M. Calabrese. "Di_usion tensor magnetic resonance imaging of the normal breast: reproducibility of DTI-derived fractional anisotropy and apparent di_usion coe_cient at 3.0 T". La Radiologia Medica, 117(6):992-1003, September 2012.
[53] Savannah C. Partridge, Ali Ziadloo, Revathi Murthy, Steven W. White, Sue Peacock, Peter R. Eby, Wendy B. DeMartini, and Constance D. Lehman. "Diffusion tensor MRI: preliminary anisotropy measures and mapping of breast tumors". Journal of magnetic resonance imaging: JMRI, 31(2):339-347, February 2010.

[54] Pascal A. T. Baltzer, Anja Schafer, Matthias Dietzel, David Gr• assel, Mieczyslaw Gajda, Oumar Camara, and Werner A. Kaiser. "Diffusion tensor magnetic resonance imaging of the breast: a pilot study". European Radiology, 21(1):1-10, January 2011.
[55] Erez Eyal, Myra Shapiro-Feinberg, Edna Furman-Haran, Dov Grobgeld, Talia Golan, Yacov Itzchak, Raphael Catane, Moshe Papa, and Hadassa Degani. "Parametric diffusion tensor imaging of the breast". Investigative Radiology, 47(5):284-291, May 2012.
[56] J. R. Buscombe, J. B. Cwikla, D. S. Thakrar, and A. J. Hilson. "Scintigraphic imaging of breast cancer: a review". Nuclear Medicine Communications, 18(8):698{709, August 1997.
[57] Renee M. Moadel. "Breast cancer imaging devices". Seminars in Nuclear Medicine, 41(3):229-241, May 2011.
[58] S. R. Cherry, J. A. Sorenson, and M. E. Phelps. "Physics in Nuclear Medicine". Philadelphia, PA: Saunders, 4th edition, 2012.
[59] Isabelle Mathieu, Stephane Mazy, Bernard Willemart, Michel Destine, Gilbert Mazy, and Max Lonneux. "Inconclusive triple diagnosis in breast cancer imaging: is there a place for scintimammography?". Journal of Nuclear Medicine: Official Publication, Society of Nuclear Medicine, 46(10):1574-1581, October 2005.
[60] Silvana Del Vecchio, Antonella Zannetti, Andrea Ciarmiello, Luigi Aloj, Corradina Carac_o, Rosa Fonti, Gerardo Botti, Giuseppe D'Aiuto, and Marco Salvatore. "Dynamic coupling of 99mTc-MIBI efflux and apoptotic pathway activation in untreated breast cancer patients". European Journal of Nuclear Medicine and Molecular Imaging, 29(6):809-814, June 2002.
[61] Terez Marian, Laszlo Balkay, Gabor Szabo, Zoard T. Krasznai, Zoltan Hernadi, Laszlo Galuska, Judit Szabo-Peli, Olga Esik, Lajos Tron, and Zoltan Krasznai. "Biphasic accumulation kinetics of [^{99m}Tc]-hexakis-2-methoxyisobutyl isonitrile in tumour cells and its modulation by lipophilic P-glycoprotein ligands". European Journal of Pharmaceutical Sciences: Official Journal of the European Federation for Pharmaceutical Sciences, 25(2- 3):201-209, June 2005.
[62] B.C. Pieper, J.E. Bowsher, M.P. Tornai, G. Peter, K. Greer, and R.J. Jaszczak. "Breast tumor imaging using a tiltable head SPECT camera". IEEE Transactions on Nuclear Science, 48(4):1477-1482, August 2001.
[63] C. Scarfone, R. J. Jaszczak, J. Li, M. S. Soo, M. F. Smith, K. L. Greer, and R. E. Coleman. "Breast tumour imaging using incomplete circular orbit pinhole SPET: a phantom study". Nuclear Medicine Communications, 18(11):1077-1086, November 1997.
[64] A. Seret, M. Defrise, and D. Blocklet. "180 degree pinhole SPET with a tilted detector and OS-EM reconstruction: phantom studies and potential clinical applications". European Journal of Nuclear Medicine, 28(12):1836-1841, December 2001.
[65] H. Wang, C. Scarfone, K.L. Greer, R.E. Coleman, and R.J. Jaszczak. "Prone breast tumor imaging using vertical axis-of-rotation (VAOR) SPECT systems: an initial study". IEEE Transactions on Nuclear Science, 44(3):1271-1276, June 1997.
[66] J.E. Bowsher, M.P. Tornai, S.D. Metzler, J. Peter, and R.J. Jaszczak. "SPECT breast imaging using more nearly complete orbits and combined pinhole-parallel-beam collimation". volume 3, pages 1328-1330. IEEE, 2002.
[67] M. Singh and E. Mumcuoglu. "Design of a CZT based breast SPECT system". volume 2, pages 1150-1154. IEEE, 1997.
[68] Martin P. Tornai, James E. Bowsher, Caryl N. Archer, J• org Peter, Ronald J. Jaszczak, Lawrence R. MacDonald, Bradley E. Patt, and Jan S. Iwanczyk. "A 3D gantry single photon emission tomograph with hemispherical coverage for dedicated breast imaging". Nuclear Instruments and Methods in Physics Research Section A: Accelerators, Spectrometers, Detectors and Associated Equipment, 497(1):157-167, January 2003.

[69] M.P. Tornai, C.N. Brzymialkiewicz, S.J. Cutler, and P. Madhav. "Comparison of scintimammography and dedicated emission mammotomography". volume 5, pages 2818-2822. IEEE, 2004.
[70] Usmani S, Niaz K, Maseeh-Uz-Zaman, Niyaz K, Khan HA, Habib S, Kamal S (2007) Chest wall recurrence of breast cancer demonstrated on 99mTc-MIBI scintimammography. Nucl Med Commun 28:842–846.
[71] C. J. Thompson, K. Murthy, I. N. Weinberg, and F. Mako. "Feasibility study for positron emission mammography". Medical Physics, 21(4):529-538, April 1994.
[72] K. Murthy., M. Aznar, C. J. Thompson, A. Lout, R. Lisbona, and J. H. Gagnon. "Results of preliminary clinical trials of the positron emission mammography system PEM-I: a dedicated breast imaging system producing glucose metabolic images using FDG". Journal of Nuclear Medicine: O_cial Publication, Society of Nuclear Medicine, 41(11):1851-1858, November 2000.
[73] Irving N. Weinberg, David Beylin, Valera Zavarzin, Steve Yarnall, Pavel Y. Stepanov, Edward Anashkin, Deepa Narayanan, Sergei Dolinsky, Kathrin Lauckner, and Lee P. Adler. "Positron emission mammography: high-resolution biochemical breast imaging". Technology in Cancer Research & Treatment, 4(1):55-60, February 2005.
[74] D. W. Townsend, "Multimodality imaging of structure and function". Phys. Med. Biol., vol. 53, no. 4, pp. R1–R39. 2008;
[75] Cherry S. R. "Multimodality imaging: beyond PET/CT and SPECT/CT". Seminars in Nuclear Medicine. vol 39 (Amsterdam: Elsevier) pp 348–53. 2009;
[76] Vandenberghe S., Marsden P.K. "PET–MRI: a review of challenges and solutions in the development of integrated multimodality imaging." Phys Med Biol 60:R115–R154. 2015.
[77]http://www.fda.gov/Radiation-EmittingProducts/RadiationEmittingProductsandProcedures/MedicalImaging/MedicalX-Rays/ucm115318.htm. Last accessed in 25th February, 2016
[78] http://www.impactscan.org/CThistory.htm. Last accessed in 25th February, 2016
[79] X-Ray Computed Tomography in Biomedical Engineering (book)
[80] W.A.Kalender. "X-raycomputedtomography". Phys.Med.Biol.51(13)(2006), R29–R43.
[81] http://www.mayoclinic.org/tests-procedures/ct-scan/basics/definition/prc-20014610. Last accessed in 25th February, 2016
[82] http://recil.grupolusofona.pt/bitstream/handle/10437/5501/computer_tomography_scanners_portugal.pdf?sequence=1. Last accessed in 25th February, 2016
[83] J. Hsieh. "Computed Tomography: Principles, Design, Artifacts, and Recent Advances". Hoboken, New Jersey: John Wiley & Sons, Inc., 2nd edition, 2009.
[84] Jerrold T. Bushberg, J. Anthony Seibert, Edwin M. Leidholdt Jr., and John M. Boone. "The Essential Physics of Medical Imaging". Philadelphia, PA: Lippincott Williams & Williams, 3rd edition, 2011.
[85] Rolf Behling. "Modern Diagnostic X-Ray Sources: Technology, Manufacturing, Reliability". CRC Press. June 26, 2015
[86] Philip Palin Dendy, Brian Heaton. "Physics for Diagnostic Radiology." CRC Press. August 4, 2011.
[87] R.J. Jaszczak. "The early years of single photon emission computed tomography (SPECT): an anthology of selected reminiscences". Phys Med Biol, 51, p. R99. 2006.
[88] G. L. Zeng, "Single-Photon Emission Computed Tomography," Emission tomography: the fundamentals of PET and SPECT, M. N. Wernick and J. N. Aarsvold, eds., pp. 127-152: Elsevier Academic Press, 2004.
[89] C. B. Hruska, and M. K. O'connor, "Nuclear imaging of the breast: Translating achievements in instrumentation into clinical use," Medical Physics, vol. 40, no. 5, May, 2013.

[90] Bucerius, Jan, Ahmadzadehfar, Hojjat, Biersack, Hans-Jürgen. “99mTc-Sestamibi Clinical Applications”. Spinger, 2012.
[91] Miles N. Wernick, and John N. Aarsvold. “Emission Tomography. The Fundamentals of PET and SPECT”. Elsevier, 2004.
[92] Carmen Bouckaert, Stefaan Vandenberghe, and Roel Van Holen. "Evaluation of a compact, high-resolution SPECT detector based on digital silicon photomultipliers". Physics in Medicine and Biology, 59(23):7521{7539, December 2014.
[93] T. E. Peterson, and L. R. Furenlid, “SPECT detectors: the Anger Camera and beyond,” Physics in Medicine and Biology, vol. 56, no. 17, pp. R145-R182, Sep 7, 2011.
[94] B. F. Hutton, “New SPECT technology: potential and challenges,” Eur J Nucl Med Mol Imaging, vol. 37, no. 10, pp. 1883-1886, Oct 20, 2010.
[95] C. Levin, "Application-Specific Small Field-of-View Nuclear Emission Imagers in Medicine," Emission tomography: The fundamentals of PET and SPECT, M. N. Wernick and J. N. Aarsvold, eds., pp. 293-334: Elsevier Academic Press, 2004.
[96] Ricardo Capote. " Single Photon Emission Mammography with Convergent Collimators". PhD thesis, in Biomedical Engineering. University of Lisbon. 2015.
[97] G. F. Knoll. "Radiation detection and measurement". John Wiley & Sons, Inc., 4th edition, 2010.
[98] B.J. Pichler and J.B. Ziegler. ""Photodetectors," in Emission Tomography: The Fundamentals of Pet and SPECT, M. N. Wernick and J. N. Aarsvold". Eds. Amerstdam: Elsevier Academic Press, 2004.
[99] Charlotte Robert, Guillaume Montemont, Veronique Rebu el, Lock Verger, and Irene Buvat. "Optimization of a parallel hole collimator/CdZnTe gamma-camera architecture for scintimammography". Medical Physics, 38(4):1806{1819, April 2011.
[100] R. A. Powsner, and E. R. Powsner, "Nonimaging scintillation detectors," Essentials of Nuclear Medicine Physics, pp. 52-64: Wiley, 1998.
[101] H. O. Anger, “Use of a Gamma-Ray Pinhole Camera for Invivo Studies,” Nature, vol. 170, no. 4318, pp. 200-201, 1952.
[102] H. O. Anger, “Scintillation Camera with Multichannel Collimators,” J. Nucl. Med., vol. 5, no. 7, pp. 515-531, Jan 1, 1964.
[103] G. Gullberg, G. Zeng, F. Datz, P. Christian, C. Tung, and H. Morgan, “Review of convergent beam tomography in single photon emission computed tomography,” Phys. Med. Biol., vol. 37, no. 3, pp. 507-534, Jan 1, 1992.
[104] P. Berthout, J. Cardot, R. Faivre, Y. Bernard, M. Baud, A. Jouan, J. Verdenet, J. Bassand et al., “Compasison between vertical parallel hole collimator and 30-degrees rotating slant hole collimator for assessing global and regional left-ventricular function by radionuclide angiography,” Eur J Nucl Med, vol. 14, no. 3, pp. 120-124, Jan 1, 1988.
[105] F. Beekman, and F. van der Have, “The pinhole: gateway to ultra-high-resolution threedimensional radionuclide imaging,” European Journal of Nuclear Medicine and Molecular Imaging, vol. 34, no. 2, pp. 151-61, Feb, 2007.
[106] D. L. Gunter, "Collimator Design for Nuclear Medicine," Emission tomography: the fundamentals of PET and SPECT, M. N. Wernick and J. N. Aarsvold, eds., pp. 153-168: Elsevier Academic Press, 2004.
[107] H. Wieczorek, and A. Goedicke, “Analytical model for SPECT detector concepts,” IEEE Trans. Nucl. Sci., vol. 53, no. 3, pp. 1102-1112, Jan 1, 2006.
[108] R. F. Brem, J. M. Schoonjans, D. A. Kieper, S. Majewski, S. Goodman, and C. Civelek, “Highresolution scintimammography: a pilot study,” Journal of nuclear medicine : official publication, Society of Nuclear Medicine, vol. 43, no. 7, pp. 909-15, Jul, 2002.

[109] C. B. Hruska, S. W. Phillips, D. H. Whaley, D. J. Rhodes, and M. K. O'Connor, "Molecular Breast Imaging: Use of a Dual-Head Dedicated Gamma Camera to Detect Small Breast Tumors," American Journal of Roentgenology, vol. 191, no. 6, pp. 1805-1815, Dec, 2008.
[110] http://pt.medwow.com/med/gamma-camera-mobile/dilon-technologies/6800/34159.model-spec. Last accessed 25th February 2016.
[111] http://www.lymphotec.co.jp/wp/wp-content/themes/lymphotec-child/images/en/mb_imaging/Data-Sheet.pdf. Last accessed 25th February 2016.
[112] http://www.medwow.com/med/gamma_camera_mobile/gamma_medica/lumagem_3200s/7125.model-spec. Last accessed 25th February 2016.
[113] M. O'Connor, D. Rhodes, C. Hruska, S. Phillips, and D. Whaley, "Molecular breast imaging (MBI) as an adjunct to screening mammography," J NUCL MED MEETING ABSTRACTS, vol. 49, no. MeetingAbstracts_1, pp. 40P-b-, May 1, 2008, 2008.
[114] M. K. O'Connor, G. Tourassi, and C. G. Orton, "Point/counterpoint. Molecular breast imaging will soon replace x-ray mammography as the imaging modality of choice for women at high risk with dense breasts," Medical Physics, vol. 36, no. 5, pp. 1463-6, May, 2009.
[115] D. J. Rhodes, C. B. Hruska, S. W. Phillips, D. H. Whaley, and M. K. O'Connor, "Dedicated Dual-Head Gamma Imaging for Breast Cancer Screening in Women with Mammographically Dense Breasts," Radiology, vol. 258, no. 1, pp. 106-118, Jan 1, 2011.
[116] M. O'Connor, D. Rhodes, and C. Hruska, "Molecular breast imaging," Expert review of anticancer therapy, vol. 9, no. 8, pp. 1073-80, Aug, 2009.
[117] Bruyant PP. "Analytic and iterative reconstruction algorithms in SPECT". J Nucl Med 43(10):1343–1358. 2002
[118] Nargol Rezvani. "Iterative Reconstruction Algorithms for Polyenergetic X-Ray Computerized Tomography". PhD thesis. University of Toronto. 2012;
[119] Hudson, H.M., Larkin, R.S. (1994) "Accelerated image reconstruction using ordered subsets of projection data", IEEE Trans. Medical Imaging, 13 (4), 601–609.
[120] Buvat, I., Monte Carlo simulations in SPET and PET. Quarterly Journal of Nuclear Medicine 46, 48-61 (2002).
[121] Stan Ulam, John Von Neuman, and the Monte Carlo Method by Roger Eckhardt https://www.fas.org/sgp/othergov/doe/lanl/pubs/00326867.pdf. Retrieved 10th September 2016.
[122] Luis Peralta. "Introdução aos métodos de simulação Monte Carlo no transporte de radiação". January 2010.
[123] "MCNP6.1 home Page". LANL. 5 August 2013. Archived from the original on March 30, 2012. Retrieved 13th September 2016.
[124] Agostinelli, S.; Allison, J.; Amako, K.; Apostolakis, J.; Araujo, H.; Arce, P.; Asai, M.; Axen, D.; et al. (2003). "Geant4—a simulation toolkit". Nuclear Instruments and Methods in Physics Research Section A: Accelerators, Spectrometers, Detectors and Associated Equipment. 506 (3): 250.
[125] Baro J., J. Sempau, J.M. Fernández-Varea and F. Salvat (1995), "PENELOPE: an algorithm for Monte Carlo simulation of the penetration and energy loss of electrons and positrons in matter", Nucl. Instrum. Meth. B 100, 31–46.
[126] University of Washington. SimSET Home Page. Available at http://depts.washington.edu/simset/html/simset_main.html. Retrieved 13th September 2016.
[127] Jan S et al. "GATE: a simulation toolkit for PET and SPECT". Phys. Med. Biol. 49 4543–61. 2004
[128] G. Marsaglia and A. Zaman, "Monkey tests for random number generators," Comput. Math. Appl. 23, 1–10, 1993

[129] Karine Assie, Vincent Breton, Irene Buvat, Claude Comtat, S_ebastien Jan, Magalie Krieguer, Delphine Lazaro, Christian Morel, Martin Rey, Giovanni Santin, Luc Simon, Steven Staelens, Daniel Strul, Jean-Marc Vieira, and Rik Van de Walle. "Monte Carlo simulation in PET and SPECT instrumentation using GATE". Nuclear Instruments and Methods in Physics Research Section A: Accelerators, Spectrometers, Detectors and Associated Equipment, 527(1-2):180-189, July 2004.
[130] S. Jan, G. Santin, D. Strul, S. Staelens, K. Assi_e, D. Autret, S. Avner, R. Barbier, M. Bardi_es, P. M. Bloom_eld, D. Brasse, V. Breton, P. Bruyndonckx, I. Buvat, A. F. Chatziioannou, Y. Choi, Y. H. Chung, C. Comtat, D. Donnarieix, P. Descourt, L. Ferrer, S. J. Glick, C. J. Groiselle, D. Guez, P.-F. Honore, S. Kerhoas-Cavata, A. S. Kirov, V. Kohli, M. Koole, M. Krieguer, D. J. van der Laan, F. Lamare, G. Largeron, C. Lartizien, D. Lazaro, M. C. Maas, L. Maigne, F. mayet, F. Melot, C. Merheb, E. Pennacchio, J. Perez, U. Pietrzyk, F. R. Rannou, M. Rey, N. Rehfeld, D. R. Schaart, C. R. Schmidtlein, L. Simon, S. Stute, T. Y. Song, J.-M. Vieira, D. Visvikis, R. Van de Walle, E. Wieers, and C. Morel. "GATE Users Guide Version 5.0.0", June 2009.
[131] Gustav Ullman, Michael Sandborg, Roger Hunt, David R Dance and Gudrun Alm Carlsson. “Implementation of pathologies in the Monte Carlo model in chest and breast imaging”. Report 94 Dec. 2003 ISRN ULI-RAD-R--94—SE.
[132] PaxScan® 2520D/CL Amorphous Silicon Digital X-Ray Imager – Product Description http://www.xrayllc.com/PaxScan2520D.pdf. Retrieved 20th November 2014.
[133] Evans P. “Calculation of x-ray spectra emerging from an x-ray tube. Part I. Electron penetration characteristics in x-ray targets.” Med. Phys. 34 2164–74. 2007
[134] Poludniowski G. “Calculation of x-ray spectra emerging from an x-ray tube. Part II. X-ray production and filtration in x-ray targets.” Med. Phys. 34 2175–86. 2007